



University of
Massachusetts
Amherst

Buckling of Particle-Laden Interfaces

Item Type	thesis
Authors	Dias Kassuga, Theo
DOI	10.7275/5752362
Download date	2024-11-26 13:36:34
Link to Item	https://hdl.handle.net/20.500.14394/33876

BUCKLING OF PARTICLE-LADEN INTERFACES

A Thesis Presented

by

THEO DIAS KASSUGA

Submitted to the Graduate School of the
University of Massachusetts Amherst in partial fulfillment
of the requirements for the degree of

MASTER OF SCIENCE IN MECHANICAL ENGINEERING

September 2014

Department of Mechanical and Industrial Engineering

BUCKLING OF PARTICLE-LADEN INTERFACES

A Thesis Presented

by

THEO DIAS KASSUGA

Jonathan P. Rothstein, Chair

Ashwin Ramasubramaniam, Member

Benjamin Davidovitch, Member

Donald Fisher, Department Head
Department of Mechanical and Industrial Engineering

ABSTRACT

BUCKLING OF PARTICLE-LADEN INTERFACES

SEPTEMBER 2014

THEO DIAS KASSUGA, B.S, UNIVERSIDADE FEDERAL FLUMINENSE

M.S.M.E., UNIVERSITY OF MASSACHUSETTS, AMHERST

Directed by: Professor Jonathan P. Rothstein

We study the buckling of an oil-water interface populated by micron-sized latex particles using a Langmuir trough. We extend pre-existing results to the micron-range with different capillary length and compare the experimental data to the existing theoretical framework. An unexpected trend for the dominant wavelength of buckling is observed, suggesting that there is a transition between regimes in the micron-range. A mechanism for the new regime is proposed. Cascading is reported, as well as novel kinds of transition between wavelengths within the same particle raft. Lastly, the effect of compression on the macroscopic arrangement of particles is investigated, as well as its effect on the buckling wavelength.

TABLE OF CONTENTS

	Page
LIST OF TABLES	v
LIST OF FIGURES	vi
CHAPTER	
1. INTRODUCTION	1
1.1 Particle-laden Interfaces.....	1
1.2 Buckling.....	8
1.3 Motivation.....	11
1.4 Literature review.....	14
1.5 Objectives	18
2. THEORY	20
2.1 Buckling wavelength and its relation to the mechanical properties of the particle raft	20
2.2 Particle-particle interactions	23
3. MATERIALS AND METHODS.....	26
4. RESULTS AND DISCUSSION.....	35
4.1 Regime transition	35
4.2 Cascading and branching	47
4.3 Hysteresis	58
5. CONCLUSION.....	69
APPENDIX: C++ CODE.....	71
BIBLIOGRAPHY	75

LIST OF TABLES

Table	Page
3-1: Properties of the particles used in the present work.	31
3-2: Engineering strain as a function of step.	34

LIST OF FIGURES

Figure	Page
1-1: Oil droplets in water. a) A small droplet will remain spherical due to surface tension; b) A larger drop becomes elongated due to flotation, a gravity-induced phenomenon.	2
1-2: Solid spheres on an oil-water interface.	3
1-3: Different regimes for particles on a fluid-liquid interface, not to scale. a) Particles adsorb and desorb reversibly; b) Particles adsorb irreversibly but cause little interfacial deformation; c) Particles adsorb irreversibly with considerable interfacial deformation; d) Particles do not adsorb to the interface, floating or sinking depending on their density.	6
1-4: 3.1 μm polystyrene particles at a hexadecane-water interface. Image obtained using a scanning electron microscope and a gelation technique proposed by (Paunov, 2003).	7
1-5: A particle-laden interface approaching buckling. a) Low surface coverage, particles are relatively free to move in 2D; b) Particles are jammed, onset of buckling.	8
1-6: Catastrophic buckling of a soda straw. a) Uniaxial compression; b) Onset of buckling; c) Energy is focused into a fold - structural failure.	9
1-7: Buckling of a slender object under uniaxial compression and hinge boundary conditions. Note that only half a wavelength is covered within the domain.	10
1-8: Buckling with a vertical restoring force (right) compared to buckling without a restoring force (left).	10
1-9: Relevant variables in buckling of particle-laden interfaces.	11
2-1: Reasoning behind the assumption for Poisson ratio. As the sheet is compressed, two triangular cells develop into a rhombohedral cell.	22
3-1: Schematic representation of the Langmuir trough.	26
3-2: Diagram of experimental method. I, II and III) Spreading the particles on the decane-water interface; IV) Compressing the interface with the moving wall; V) Obtaining images using a CMOS camera, a laser and a moving stage; VI) Combining images to form a single picture of the interface.	29
3-3: Image processing for each part of the present work. A-VII) Hysteresis; B-VII) Measuring wavelength directly for regime transition; C-VII) Cascading.	30

3-4: Lycopodium powder (left) and 10 μm latex particles (right) under an optical microscope. The latex particles are clearly spherical, while the lycopodium particles are bullet-shaped.	32
3-5: Average circularity of lycopodium particles compared to the circularities of a square, a regular octagon and a circle.	33
4-1: Wavelength as a function of diameter.	35
4-2: Fractal formation of lycopodium particles on an air-water interface.	37
4-3: Lycopodium particles on a buckled air-water interface.	37
4-4: 0.1 μm -particle raft under compression. At step 5 (32% strain), the interface is flat. It is compressed to step 7 (81% strain), where buckling is widespread. Then, the interface is stretched to step 8 (0% strain) and back to step 9 (32% strain). At step 9, stacks of particles can be observed as bright stripes approximately perpendicular to the direction of compression.	39
4-5: Trilayer unfolding upon release of compression. Lycopodium on an air-water interface.	40
4-6: Buckling of a 1.8- μm -particle raft: a) Wrinkling starts near the moving wall, with shear from the side walls; b) Folds form near the moving wall, wrinkles develop in the middle of the sheet, where shear seems less pronounced.	41
4-7: Schematic of the development of folds: a) An interface populated with particles (not shown) before compression; b) If the bending stiffness is low, the interface folds upon itself, forming a trilayer; c) Trilayers subsequently buckle at a higher wavelength; d) If the bending stiffness is high, a wrinkle develops and no trilayers form; e) Further compression leads to folding near the moving wall; f) New wrinkles form beyond the fold.	43
4-8: Wavelength as a function of step in experimental protocol (see Table 3-2 for corresponding strain), for the 0.1 μm and 0.5 μm cases.	45
4-9: Wavelength as a function of diameter. Squares show original data, triangles show data for 0.1 μm and 0.5 μm after the diameter shift. The dashed line is a fit with exponent 0.5 over the adjusted data ($r^2=0.73$). The circles represent step 5 (32% strain) for 0.1 μm and step 2 (15% strain) for 0.5 μm	46
4-10: A 0.5- μm -particle raft under compression. Note that wrinkles occur in different wavelengths at different parts of the raft.	48
4-11: Wavelength transition events in particle-laden interfaces: a) A wrinkle splits into two wrinkles, 1.8-micron-particle raft; b) Wrinkles end abruptly at the end of a buckled area, while other wrinkles split before ending, 0.8-micron-particle raft; c) A wrinkle splits into five wrinkles at the edge of a buckled	

area, 0.5-micron-particle raft; d) The transition between the wrinkles at the top and bottom occurs through a flat area, 1.0-micron-particle raft; e) Fault-like transition on a 0.8-micron-particle raft; f) Gradual transition from a large wavelength to a much smaller wavelength, then a sudden transition to flat, 2.9-micron-particle raft.	50
4-12: Edge of a wrinkled region on an air-water interface populated by lycopodium particles.	53
4-13: Example of cascading (left) and corresponding image processing output (right, wavelengths in grayscale code) on a 1.025 μm particle raft.	54
4-14: The buckled section of a particle raft divided into different transition events (top), and the wavelength as a function of the distance perpendicular to compression (bottom) with power law fits. Events: 1 – smooth (“heavy sheet”) cascading; 2 – constant wavelength; 3, 4, 5, 6 and 7 – sharp transitions; 8 – sharp (“light sheet”) cascading.	55
4-15: Histogram of exponent m for all cascading events recorded.	56
4-16: Statistics for exponent m as functions of particle diameter.	57
4-17: Hysteresis on a 1.8 μm -particle raft, numbers represent step in protocol (all at 32% strain).	59
4-18: The fraction of the particle-laden interface that is buckled (Q , squares) and engineering strain (columns) as a function of step within the experimental protocol, for each particle diameter.	61
4-19: 2.9-micron interface at step 1. While buckling occurs at the top part of the image, most of the interface remains flat, indicating that the particle distribution is uneven on the interface.	63
4-20: 1.0-micron interface at step 1. Regions of particle depletion can be clearly seen as dark areas on the image.	64
4-21: Wavelength (squares) and engineering strain (columns) as a function of step for each particle diameter.	66
4-22: 31 μm -particle raft at steps 5, 7 and 9.	67
6-1: Parameters for calculating the buckling wavelength; 2.9 μm -particle raft.	72

CHAPTER 1

INTRODUCTION

1.1 Particle-laden Interfaces

When a fluid (gas or liquid) and a liquid come into contact, a region of transition between the two can be devised: a fluid-liquid interface. At the interface, molecules of both fluids interact, so that it is in fact a diffuse mixture of both fluids (Birdi, 1999). However, to the casual observer of fluid interfaces in everyday life situations (such as oil and water in a pot or air bubbles in water) the interface may seem to be an infinitely thin surface. Indeed, fluid interfaces have been successfully described as 2D membranes (Birdi, 1999).

These interfaces are characterized by a sharp change in fluid properties, either from a liquid to a liquid of different composition or from a liquid to a gas. This means that molecules along the interface must interact with molecules of the different fluid, or of the same fluid in a different phase; naturally, that means they are under different forces than their counterparts farther into the bulk (Birdi, 1994) (de Gennes, Brochard-Wyart, & Quere, 2003). Therefore, the cohesion between molecules on each side of the interface tends to be smaller than the cohesion between molecules in each bulk fluid. Consequently, molecules within a fluid will pull each other closer, which at continuum scale means the fluids tend to minimize the contact area with each other. In other words, the interface “wants” to be as small as possible, or to contract (Birdi, 1999).

This could lead to the conclusion that fluids will always assume a spatial configuration that reduces the interfacial area. However, that is not always the case; for example, while small oil droplets will remain spherical when attached to the walls of a glass of water, larger droplets will bend in more complex shapes, or even separate from the

wall and float upwards in fairly complex motion (see Figure 1-1 for an example). What this shows is that the actual behavior of an interface is given by the interplay of several different forces (de Gennes et al., 2003), such as the ones of gravitational and viscous nature. Therefore, a way to quantify how cohesive a fluid is when in contact with another one is necessary; that theoretical void is filled by surface tension.

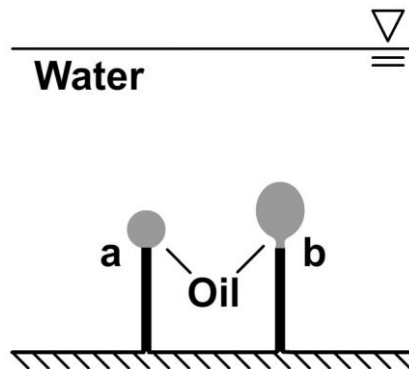


Figure 1-1: Oil droplets in water. a) A small droplet will remain spherical due to surface tension; b) A larger drop becomes elongated due to flotation, a gravity-induced phenomenon.

Surface tension is the quantification of the tendency of the interface to become smaller, i.e. its contractive tendency. It can be thought of as the surface energy per unit area of the interface, or the surface energy density (de Gennes et al., 2003). Then, the tendency of the interface to reduce its area can be thought of as a tendency to reduce the interfacial energy of the system. This leads back to the varied shapes that are observed in droplets: while in small droplets surface tension is dominant, leading to spherical shapes, in larger droplets other forms of energy must be taken into account (for example, gravity) (de Gennes et al., 2003). Thus, a large spherical droplet may be so unfavorable from a gravitational perspective that a compromise in shape is made in order to minimize the total

energy of the system, even though the surface energy of the system will increase. In Figure 1-1, droplet “a” is spherical, so it has the smallest surface-to-volume ratio possible. That is, it is optimized for surface energy minimization. Droplet “b”, on the other hand, is no longer spherical because that would increase the gravitational energy of the system considerably. Thus, it takes on a complex shape, where more of its volume is at smaller depth, at the expense of a slight increase in surface energy.

While the discussion so far has focused on fluid-liquid interfaces, interfaces between fluids and solids also have an associated surface energy density. Thus, when a solid and a fluid are in contact, there is a tendency to reduce the interface between them. Solids can resist changes in shape, so this is effectively negligible when a solid is immersed in a bulk of fluid. Nevertheless, it becomes important for solids neighboring fluid-liquid interfaces, because the shape of the interface between the two fluids can be strongly affected. The surface energy between the solid and each fluid is different, which means that the minimization of surface energy becomes a balance of how much interfacial area each one of the components has with each other (de Gennes et al., 2003). Figure 1-2 is a representation of how solid spheres may behave at an oil-water interface.

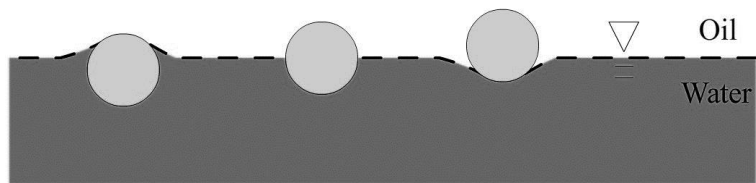


Figure 1-2: Solid spheres on an oil-water interface.

In Figure 1-2, the three spheres are depicted in decreasing affinity to water, from left to right. That is, the rightmost sphere is the most hydrophobic of the group. As the energy required to be in contact with water increases (going rightward), the sphere tends to immerse itself further in oil.

Naturally, this reasoning neglects the effects of gravity. Indeed, floating in most real-life situations is a gravity-related phenomenon where objects only float if they are less dense than water, and surface tension effects are negligible. There are exceptions, however: paper clips can float in water, as well as some species of insect (such as water striders), despite being denser than water. These exceptions occur at very small scale, which indicates that size is a determinant factor in floating (Vella, 2007). Indeed, the spheres in Figure 1-2 will only exhibit the depicted behavior if they are very small. Otherwise, gravity would become important and the spheres would either float or sink (unless they happened to be less dense than water and denser than the oil).

Yet, rigorously speaking any solid can float in any liquid due to surface tension alone, but that may require an enormous perimeter for surface tension to act upon, which makes it effectively impractical. In fact, most examples in nature are either cylindrical (legs of the water strider) or relatively simple 3D solids (ground coffee floating in water), although complex microstructures may be present. Therefore, it can be assumed that solids will only attach to a fluid-liquid interface through surface tension effects if they are small enough for gravity to be negligible. Whether something is “small” or “large” depends on how it compares to the capillary length of the interface (de Gennes et al., 2003), which is defined as:

$$L_g = \sqrt{\frac{\gamma}{(\rho_1 - \rho_2)g}} \quad (1-1)$$

where γ is the surface tension of the interface, g is the gravitational acceleration and ρ_1 and ρ_2 are the densities of the heavier and lighter fluids, respectively. For a water-air interface, this is about 2 mm, while for an oil-water interface it is around 4 mm. The capillary length imposes a limit on the size of the objects that can adsorb to an interface under gravity (Vella, 2007); this should not be taken as an absolute limit, but as an indication of order of magnitude.

Still, gravity and surface tension are not the only defining factors on how solids and fluid-liquid interfaces interact. For very small solids, thermal fluctuations may also be important. In this case, the particle is small enough that it is considerably displaced by collisions with molecules in the fluid. This behavior is called Brownian motion. While it is negligible in most large-scale phenomena, it is very important at molecular level and can effectively push a solid particle off the fluid-liquid interface. Thus, there is also a lower limit for whether a solid particle can attach to a fluid-liquid interface directly (Birdi, 1994).

Hence, there are three possibilities of interaction between particles and interfaces:

- Reversible attachment due to thermal fluctuations in the very small particle range. In this case, particles can adsorb but are also likely to desorb by being pushed off the interface by molecules and other particles;
- Irreversible attachment in the mid-range. Here, it is energetically favorable for particles to remain adsorbed, because thermal effects are negligible and gravitational forces are much smaller than capillary forces;

- No attachment at all for very large particles, where gravity dominates. Gravity-induced floating may occur, but not adsorption proper.

Furthermore, existing work (Monteux, Jung, & Fuller, 2007) has shown that irreversible attachment can be given in two separate ways: with or without interfacial deformation. That is, particles in the upper mid-range are heavy enough to deform the interface around them, which is necessary to balance their weight, but not so heavy that they detach from the interface. On the other hand, particles in the lower mid-range will attach with negligible interfacial deformation, because their weight is very small. The different regimes are depicted in Figure 1-3.

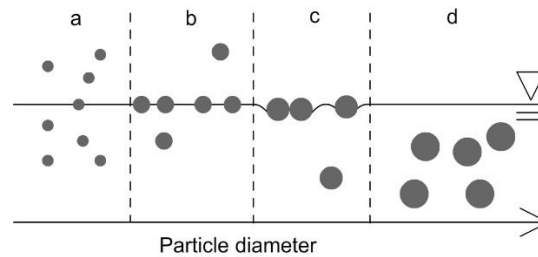


Figure 1-3: Different regimes for particles on a fluid-liquid interface, not to scale. a) Particles adsorb and desorb reversibly; b) Particles adsorb irreversibly but cause little interfacial deformation; c) Particles adsorb irreversibly with considerable interfacial deformation; d) Particles do not adsorb to the interface, floating or sinking depending on their density.

The present work is mainly concerned with regimes *b* and *c*. In regime *b*, the particles adsorb to the interface, but their effect on the shape of the interface is very limited. Therefore, capillary forces (forces due to surface tension) between particles are negligible when compared to electrostatic forces. On the other hand, both kinds of force are important in regime *c*. That can have important effects on how the interface behaves, a point which

will be discussed later in this work. Figure 1-4 shows an example of a hexadecane-water interface populated with a large number of polystyrene particles of average diameter 3.1 and 1.8 μm .

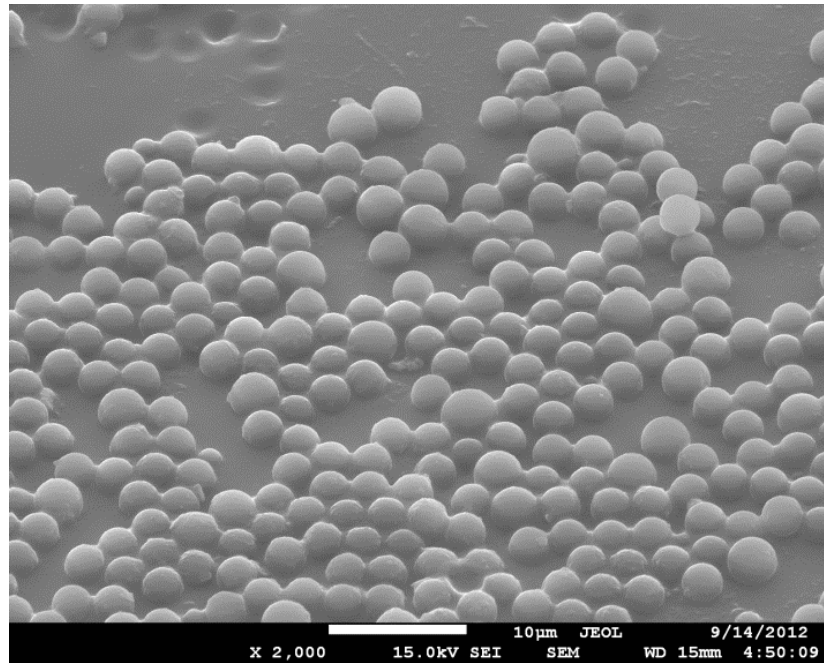


Figure 1-4: 3.1 μm polystyrene particles at a hexadecane-water interface. Image obtained using a scanning electron microscope and a gelation technique proposed by Paunov (2003).

When micron-sized particles adsorb to a fluid-liquid interface, they cannot be easily pulled off (Du, Glogowski, Emrick, Russell, & Dinsmore, 2010). Therefore, forces imposed on the interface will either cause bi-dimensional (in-plane) motion of the particles or out-of-plane deformation of the entire interface. That is, it costs less energy to rearrange or deform the interface than to make the particles desorb (Vella, Aussillous, & Mahadevan, 2004). This means that by manipulating the interface, the arrangement of the particles can be modified in 2D (see example in Figure 1-5). Furthermore, it means that the interface can

buckle out-of-plane if the interface is compressed beyond the point where the particles can rearrange in two dimensions (note that jamming does not presuppose the formation of a crystalline lattice, as defects may exist on a jammed particle structure). This is the fundamental point of the present work, but a discussion of buckling is necessary before it can be properly approached.

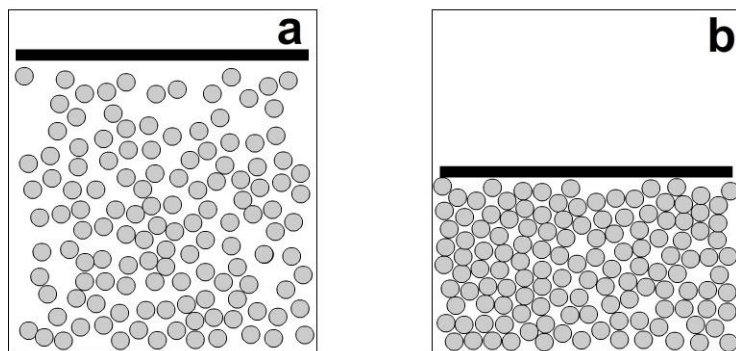


Figure 1-5: A particle-laden interface approaching buckling. a) Low surface coverage, particles are relatively free to move in 2D; b) Particles are jammed, onset of buckling.

1.2 Buckling

Buckling (or elastic instability) occurs when in-plane loads impose out-of-plane displacements on an object (Vinson, 1988). This situation is brought about when the energy cost to bend an object becomes smaller than the cost to compress it. For that reason, buckling is usually associated with slender objects, such as columns and pipes or, in a more mundane example, soda straws (Figure 1-6). Slender objects are relatively easy to bend because of their small area moment of inertia and large length.

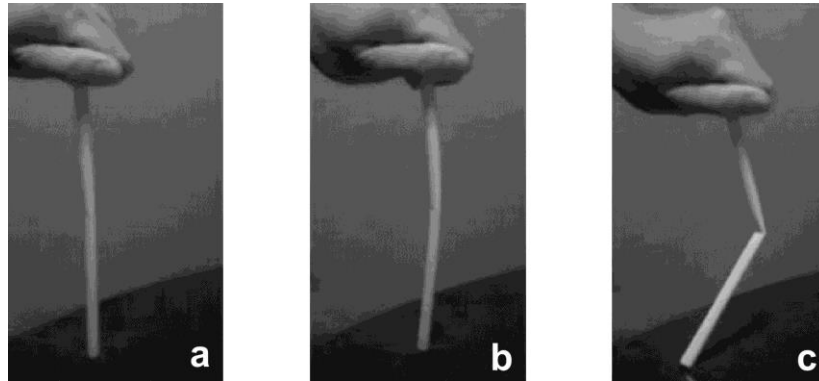


Figure 1-6: Catastrophic buckling of a soda straw. a) Uniaxial compression; b) Onset of buckling; c) Energy is focused into a fold - structural failure.

Particle-laden interfaces are certainly slender, since their thickness is of the order of the diameter of the particle (micron-scale) while the interface can measure several millimeters or more. Furthermore, the cost to compress a solid particle can be assumed to be larger than the cost to bend a liquid-fluid interface (Vella et al., 2004), which favors buckling as opposed to in-plane deformation.

The shape that an object takes upon buckling depends on a number of factors, such as: the loads it is under, the boundary conditions of the problem, the geometry of the object itself and the mechanical properties of the material (which may vary in space) (Bloom & Coffin, 2000). A particularly simple example is that of a uniformly-shaped object under uniaxial compression with hinge boundary conditions. In this case, buckling is characterized by a wavelength that equals twice the distance between the points where the compressive force is applied (Figure 1-7).



Figure 1-7: Buckling of a slender object under uniaxial compression and hinge boundary conditions. Note that only half a wavelength is covered within the domain.

In the case of particle-laden interfaces there is a restoring force (gravity) which goes against vertical displacements. This is because bending out-of-plane requires pushing fluid away from the minimum potential energy state. Consequently, gravity “wants” the interface to remain as close to the initial plane as possible. Since the length of the object is approximately constant, that would entail infinitely small wavelength and, consequently, infinitely small amplitude. However, that goes against bending energy, which requires minimization of curvature. That means a compromise between bending and gravity must be achieved, which leads to an intermediate wavelength (Figure 1-8).



Figure 1-8: Buckling with a vertical restoring force (right) compared to buckling without a restoring force (left).

This balance of competing forces can be expressed through the beam equation:

$$B \frac{\partial^4 x}{\partial x^4} + T \frac{\partial^2 x}{\partial x^2} + \rho g h = 0 \quad (1-2)$$

where B is the bending stiffness of the object (particle raft), T is the compressive force, ρ is the density difference between the liquid and the fluid, g is the gravitational acceleration and h is the vertical displacement of a point on the object compared to its

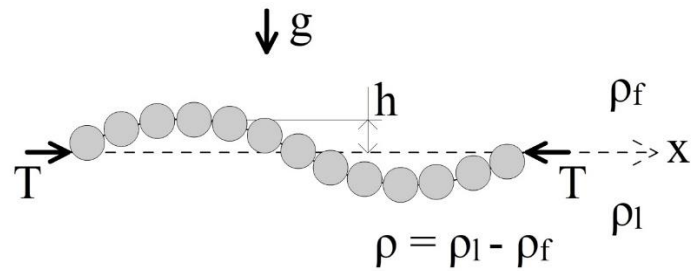


Figure 1-9: Relevant variables in buckling of particle-laden interfaces.

initial position before buckling (Figure 1-9). A derivation of the beam equation can be found in the literature (Vinson, 1988).

The importance of buckling to the study of particle-laden interfaces becomes clear through the beam equation: by looking at the geometrical response (vertical displacement field) to an imposed load (compressive force), one can attempt to understand the mechanical properties of the particle raft (bending stiffness).

Another important point is that the mechanical properties of the raft may be a function of the way the particles are arranged on the interface, as indicated by the dependence on the surface coverage ratio proposed in existing work (Vella et al., 2004). Then, looking at the geometry of the buckled interface could give insight on the packing distribution on the interface. Then, the interaction between stress, strain and packing can be observed for a wide range of configurations.

1.3 Motivation

Particle-laden interfaces have found wide application in modern industry (Binks, 2002). The most direct use for particles on interfaces is in the stabilization of emulsions, which had already been proposed in the beginning of the 20th century (Ramsden, 1903) (Pickering, 1907). Incidentally, particle-stabilized emulsions are referred to as “Pickering emulsions” in current literature.

A few factors lead to the ability of particles to stabilize emulsions. First, coalescence between drops is hindered by the presence of solids on the interfaces. Furthermore, Ostwald ripening can stop as the surface coverage ratio of smaller drops becomes higher and the effective surface tension decreases. Thus, a particle-stabilized emulsion tends to an equilibrium state where all the drops are at approximately the same Laplace pressure (Ashby & Binks, 2000). It has also been suggested that the elasticity of the particle shell around each drop could also help halt ripening by resisting compression of the drop interface (Binks, 2002). In this sense, particles and surfactant molecules have very similar effects on the behavior of the interface (Binks, 2002).

Besides stabilizing emulsions, it has been shown that particles can be used to create self-assembled capsules, for example by using a liquid jet as a template (Edmond, Schofield, Marquez, Rothstein, & Dinsmore, 2006). This opens the possibility of using particle-laden interfaces for encapsulation of active ingredients, such as drugs, by creating small, self-assembled capsules (Dinsmore et al., 2002).

However, self-assembly is not limited to curved capsules and indeed flat surfaces of different properties can be manufactured this way. It is particularly interesting that using particles of different surface treatments and of different sizes, one can trim the way they pack on the interface and thus modify the properties of the resulting solid material (Birdi, 1994). Naturally, that raises the question of how particles interact on the interface.

This question is fundamental not just for self-assembly, but also to understand the drop in surface pressure due to the presence of particles. On a very simplified level, particles interact through long and short range forces, which can be repulsive or attractive. Since a number of forces is at play at any given time (gravity, surface tension, Coulombic

attraction and repulsion, electro-dipping, etc) and they depend on a number of factors including the distance between the particles (Boneva, Christov, Danov, & Kralchevsky, 2007), it is natural to expect that the nature of these interactions can change as the packing of particles is modified.

The end result of such complex interactions is that particle-laden interfaces can have very interesting elastic behavior, particularly in shear and compression. In fact, the elasticity of the interface has been measured in a number of ways and has been shown to be affected by many of the factors already mentioned here, such as the surface properties of the particles. Furthermore, as the interface is compressed the packing density increases and eventually reaches a maximum where particles simply cannot rearrange anymore. At this point, the surface pressure tends to be zero, i.e. repulsive and attractive interactions cancel each other (Monteux, Jung, et al., 2007) (Monteux, Kirkwood, Xu, Jung, & Fuller, 2007).

Since the particles cannot rearrange, further compression must either lead to deformation of the particles themselves or out-of-plane deformation of the interface, which characterizes buckling. Since the particles tend to be much stiffer than the interface as a whole, the interface usually buckles (Vella et al., 2004) (Aveyard, Clint, Nees, & Quirke, 2000). This buckling allows for study of the mechanical properties of the particle raft, as well as understanding of the buckling phenomenon itself. This can have a number of applications in the industry, since interfaces close to buckling are the least permeable.

1.4 Literature review

The elasticity of a particle-laden interface is indicated by a drop in surface pressure upon compression as pointed out, for example, in Aveyard, Clint, Nees, & Paunov (2000). This work includes a model for particle-particle interactions at the interface, which explains the aforementioned behavior of the surface pressure. It is also shown that the arrangement of particles is affected by compression, leading to the possibility of hysteresis. Furthermore, and of particular importance to the present work, wrinkles were detected on the interface at high compressive strains. This proved that particle-laden interfaces can buckle under compression, as opposed to expelling particles into either phase. In other words, desorption does not occur.

Later, Vella et al. (2004) introduced a model for the buckling of the interface. This model relied on characterizing the particle raft as a bidimensional solid with defined Young's modulus and Poisson ratio. It should be stressed, however, that solid behavior is only expected under compression and shear, and not tension; in that case, the behavior of the raft is closer to that of a Maxwell non-Newtonian fluid, as discussed by Kang, Yeung, Foght, & Gray (2008).

By assuming that the particles are non-Brownian and interact with their immediate neighbors while in hexagonal, constant area close-packing and with wavelengths much larger than the particle diameter, Vella et al. (2004) showed that the wavelength of buckling of the interface can be predicted with good accuracy. This requires a geometrical argument for the Poisson ratio, in which the structure shifts from hexagonal to rhombohedral at the onset of buckling. These arrangements can indeed occur in particle-laden interfaces, as Aveyard, Clint, Nees, & Paunov (2000) had already shown.

Under the theory of Vella et al. (2004), the elasticity at buckling comes from the gain in area due to rearrangement of the particles. This would allow for the disappearance of the wrinkles when compression is removed, which in turn indicates that the interface has a bending stiffness. While Vella et al. (2004) obtained good results by calculating it as if the particle raft were a thin sheet of thickness equal to the diameter, empirical measurements of bending stiffness have not been done, to the best of our knowledge, due to its small magnitude. In fact, experiments done by Monteux, Jung, et al. (2007) showed that the change in surface pressure due to buckling (i.e. associated with the bending stiffness of the interface) is very small when compared to the surface pressure drop caused by initial states of compression.

This fact has also been noted by Leahy et al. (2010), where it is hypothesized that it stems from the spherical nature of the particles and, in the case of multi-layer systems, from poor coupling between layers. Incidentally, the experiments by Leahy et al. (2010) showed that nanoparticle-laden interfaces can actually fold upon themselves, forming a trilayer, and then buckle again at a considerably larger wavelength. Interestingly, the wavelength of buckling does not seem to depend on surface tension, which it did in the prediction of Vella et al. (2004).

Leahy et al. (2010) also shows that the estimates for bending stiffness under the continuum mechanics framework do not seem to apply; resistance to bending is much smaller than would otherwise be expected and drops even further if the coupling between layers is intentionally diminished. The wavelength is independent of strain and distributed around a single mode and larger folds (larger than the ones that formed the trilayers) occur as well. Furthermore, micron-sized vacancies in the crystalline lattice were observed,

which may have a negative impact on the magnitude of the Young's modulus of the particle raft.

The structure of the interface and the mechanism behind particle-particle interactions have been considered in a number of works, including the previously mentioned work by Aveyard, Clint, Nees, & Paunov (2000). That work showed that surface pressure is not isotropic for small particles (below 2 μm) and that the surface pressure curve as a function of area can give information about long range particle interactions (low slope indicates more long range interaction). The importance of surface charge is also discussed, and it is shown that sodium chloride can abate long-range repulsion by shielding the surface charges of the particles. This effect is more pronounced if the particles are more immersed in an aqueous phase, whereby more of their surface will be shielded.

Monteux, Jung, et al. (2007) investigated the behavior of bidisperse particle solutions. It was discovered that the packing of the particles and the shape of the surface pressure curve are strongly influenced by the size of the particles and the relative amount of particles of each size. In particular, it was shown that particles of a few microns in diameter do not aggregate, unless larger particles (9 μm) are present. Larger particles cause pronounced deformation of the interface, which translates into strong capillary interaction; that means more aggregation and more imperfections in the lattice, which in turn cause the surface pressure curve to look different for larger particles, when compared to the smaller ones. An important feature of this work is the suggestion of the possibility of non-negligible Brownian motion for particles below 1 μm .

Existing work is not limited to mixtures of spherical particles; for example, Kang et al. (2008) looked at hexadecane-water interfaces covered with hydrophobic bacteria.

Interestingly, the interface only seems to buckle when the bacteria have fimbriae. The proposed explanation is that the fimbriae allow connections between the bacteria, offering noticeable resistance to shear, thereby allowing buckling. Furthermore, the experimental results indicate that the bacterium-laden interface has a yield stress and that the Young's modulus increases with bacterium concentration.

Horozov, Binks, Aveyard, & Clint (2006) discussed the effects of hydrophobicity on the behavior of particle monolayers. Very hydrophobic particles form more organized monolayers, while less hydrophobic ones do not. The latter induce more interfacial deformation which leads to stronger capillary interaction, thus breaking the order of the system; conversely, the former allow long distance Coulombic interactions to take place, creating an organized lattice.

Since irregularly shaped particles were used in that work, considerable hysteresis was observed when the particle raft underwent successive compression cycles. It was found that the particles rearranged irreversibly during each compression, until they could no longer rearrange. Then, buckling occurred, first at small wavelengths, which were then superimposed by larger wavelengths (ratio of about 1:8). This can be explained by the fact that the particles form network structures that can buckle well before collapse pressure, when they buckle again (this time at larger wavelength). That indicates that the bending stiffness increases with compression. Lastly, the authors present a model for amplitude based on the wavelength and assuming a sinusoidal profile.

In a related field, Huang, Davidovitch, Santangelo, Russell, & Menon (2010) have shown that the wavelength of wrinkles on a floating thin elastic sheet decays as one moves from the center of the sheet to the border. This occurs because the sheet along the border

has to balance the capillary forces on the neighboring interface, which imposes another restoring force on the wrinkles (in addition to gravity, which also acts in the middle of the sheet). The decay of the wavelength is characterized by a smooth cascading, rather than localized branching, because surface tension pulls on the interface perpendicularly to the direction of compression. This is in sharp contrast to what is observed in curtains, for example, where tension is very small and the wrinkles branch out abruptly.

By balancing bending and tension due to surface tension, the scaling for the penetration length of the cascades into the sheet as a function of capillary length can be obtained. Along the penetration length, the wavelength of the wrinkles goes from the unidirectional buckling on the center of the sheet to the (smaller) wavelength that balances the fluid meniscus.

Later, Vandeparre et al. (2011) developed the theory for cascading based on *wrinklons*, which are defined as the localized transition region from one wavelength to another. It is shown that the scaling for wavelength as a function of distance into the sheet depends on whether the sheet is under tension or not. This is in agreement with the results from Huang et al. (2010) that were discussed before. The possibility of a transition between regimes is also discussed.

1.5 Objectives

The objective of this work is to investigate the buckling of particle-laden interfaces. Within that general field, a number of important contributions can be made:

- a) Investigation of the possible transition between regimes at micrometric diameters, which would be characterized by a change in wavelength trend when compared to

the trend predicted by the theory of Vella et al. (2004). Also, identification of the mechanism of transition, with a number of possibilities: relative intensification of Brownian motion, the formation of multilayers or the change in the relative importance of each kind of inter-particle force.

- b) Description of the mechanism behind the wavelength distribution, including the possible cascading and/or branching transitions between wavelengths. Characterization of cascading/branching in particle-laden interfaces, including scaling.
- c) Characterization of the hysteresis on spherical particle-laden interfaces through successive compression.

CHAPTER 2

THEORY

2.1 Buckling wavelength and its relation to the mechanical properties of the particle raft

As previously discussed, buckling is an elastic instability that occurs when the cost to bend something is smaller than the cost to compress it. That can mean two different things when applied to particle-laden interfaces:

- a) The cost to deform solid particles elastically is higher than the cost to move them out-of-plane;
- b) The cost to force solid particles into closer packing (higher solid area ratio) is higher than the cost to move them out-of-plane.

This distinction is important because the packing ratio at which buckling occurs affects the buckling wavelength, as will soon be discussed. Evidence so far has shown that there is a tendency for buckling to occur only when condition “a” is achieved, that is, when the interface is compressed to the point where the particles must either move out-of-plane or undergo elastic strain. This can be observed, for example, in Vella et al. (2004), Aveyard, Clint, Nees, & Paunov (2000) and Aveyard, Clint, Nees, & Quirke (2000).

Vella et al. (2004) proposed that the beam equation could be used to describe the buckling of particle-laden interfaces. It was therefore necessary to express the bending stiffness as a function of known parameters of the problem, so the following form was chosen:

$$B = \frac{Ed^3}{12(1 - \nu^2)} \quad (2-1)$$

where E is the Young's modulus, d is the diameter of the particle and ν is the Poisson ratio. This formula was borrowed from solid sheet theory and was directly adapted by substituting the thickness of the sheet by the diameter of the particles.

Then, assuming a sinusoidal profile for the geometry of the sheet:

$$h(x) = A \sin\left(\frac{2\pi x}{\lambda}\right) \quad (2-2)$$

where A is the amplitude of the wrinkles, x is the position along the direction of compression and λ is the wavelength of the wrinkles (or buckling wavelength). Now, the compressive force on the sheet can be expressed as a function of the wavelength of buckling and minimized to yield the selected wavelength:

$$\lambda = \pi \left[\frac{4Ed^3}{3\rho g(1-\nu^2)} \right]^{1/4} \quad (2-3)$$

or

$$E = \frac{3}{4\pi^4} \frac{\rho g(1-\nu^2)\lambda^4}{d^3} \quad (2-4)$$

where it should be pointed out that ρ is the density difference between the two fluids, as pointed out in Figure 1-9. This difference is always positive because the forces that make the fluid float on top of the liquid and that provide the restoring force to the particle raft are the same: gravity.

Now, the Young's modulus of the sheet can be calculated through measurements of wavelength. This is a particularly interesting point, because it allows for a geometrical, measurable property (wavelength) to be related to a mechanical and somewhat abstract property (Young's modulus).

Naturally, these expressions can only be used with prior knowledge of the Poisson ratio of the particle raft. To solve this issue, Vella et al. (2004) used a geometrical argument. Assuming that the particles are spherical and arranged in a triangular lattice, one can expect the development of two triangular cells into a rhombohedral cell when the interface is compressed, as shown in Figure 2-1.

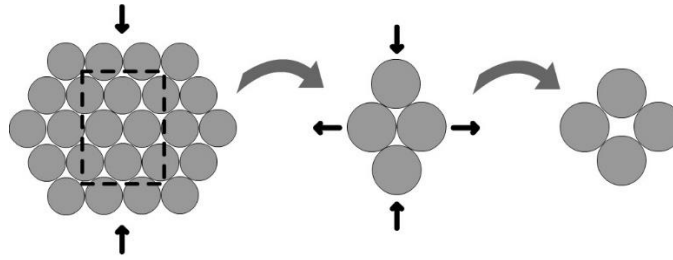


Figure 2-1: Reasoning behind the assumption for Poisson ratio. As the sheet is compressed, two triangular cells develop into a rhombohedral cell.

Then, it is easy to realize that there is a geometrical constraint on the Poisson ratio. For small deformations, the Poisson ratio can be approximated by:

$$\nu = \frac{1}{\sqrt{3}} \quad (2-5)$$

While this allows for the calculation of the Young's modulus, it does not provide a way to confirm the model other than by measuring these properties in a different experiment. In order to be able to match the model to the directly measured quantity (wavelength), a relation between the Young's modulus and other known constants was necessary. Vella et al. (2004) started by relating mean stress ($\bar{\sigma}$) to mean strain ($\bar{\epsilon}$):

$$\bar{\epsilon} = \left(\frac{1 - \nu}{E} \right) \bar{\sigma} \quad (2-6)$$

Then, considering that

$$A_l \frac{d\tau}{dA_l} \propto \gamma \quad (2-7)$$

where A_l is the area of the interface covered by liquid, τ is the thickness-averaged isotropic stress and γ is the surface tension of the fluid-liquid interface, one can obtain the following expression:

$$E \propto \left(\frac{1-\nu}{1-\phi} \right) \frac{\gamma}{d} \quad (2-8)$$

This is a scaling relation, not an equality. Thus, turning it into an equality requires choosing a proportionality constant. If that constant is set to 1, the wavelength as a function of measurable and estimated parameters becomes:

$$\lambda = \pi \left[\frac{4}{3(1-\phi)(1+\nu)} \right]^{1/4} \sqrt{L_c d} \quad (2-9)$$

where ϕ is the surface coverage ratio of solids to the entire interface. While at close packing this ratio would be about 91%, Vella et al. (2004) measured it to be around 85%. This is a particularly important parameter, however; if the mechanism of buckling changes, a change in wavelength should be expected. Consequently, understanding the nature of particle-particle interactions is necessary to understand the buckling of particle-laden interfaces, even if the latter is studied under the framework of continuum mechanics.

2.2 Particle-particle interactions

Particles at an interface are subject to a number of forces, as discussed in Boneva et al. (2007). While for large particles (several microns and larger) the effects of gravity are clearly dominant, electrostatic effects can also be pronounced for smaller particles. In

general, particles are subject to the following forces when attached to a liquid-fluid interface:

- a) Direct contact with other particles or walls of the reservoir;
- b) Capillary forces due to imposed deformation of the interface by the particles, forming capillary bridges. These forces are attractive or repulsive depending on whether the particles impose curvature of the same sign or of opposite signs, respectively (Vella & Mahadevan, 2005);
- c) Electrostatic repulsion, since particles tend to be like-charged;
- d) Electrodipping, which arises from the interaction between particle charges and the bulk fluids (Danov, Kralchevsky, & Boneva, 2004). Due to electrodipping, particles tend to sink into the interface slightly more than they would otherwise (that is, the apparent contact angle is slightly smaller than the contact angle measured on a flat surface). It is noteworthy that Paunov (2003) found the contact angle of polystyrene particles at air-water and *n*-decane-water interfaces to be smaller than that against a flat polystyrene plate. This was, however, attributed to the fact that the particles had sulfate charged groups on their surface;
- e) Electric-field-induced capillary attraction, which is probably the least intuitive among the forces mentioned here. It arises from the capillary interaction between deformations of the interface surrounding a particle. These deformations are electric-field-induced, not gravity-induced, and can occur with particles of any size. Dimples are formed around the particle, which leads to capillary bridges between dimples due to neighboring particles. The end (and somewhat unexpected) result is that like-charged particles can actually be mutually attractive solely due to their

charge, as long as they are attached to a fluid-liquid interface. Boneva et al. (2007) has shown very strong evidence that this force can have important effects on particle motion.

Because each one of these forces is favored by a different size scale, it is must be considered that they could have important effects on buckling. This is where the packing ratio becomes important in the theory of Vella et al. (2004); while it was calculated to be 85% for the relatively large particles in that work, it is possible that other values are achieved in different size-scales. In particular, the size scales in the present work are considerably smaller, as will be shown later.

This opens the possibility of a strong link between the fields of particle-particle interactions and buckling of particle-laden interfaces, where the effects of the changes in these forces may be noticeable.

CHAPTER 3

MATERIALS AND METHODS

In order to study particle-laden interfaces under different compressions, a Langmuir trough was built in acrylic. Cast acrylic was used to allow light to go through the walls, though imaging was done from above. The trough was composed of three fixed walls and a moving wall, which was controlled by hand using a micrometer. Consequently, the strain could be controlled, but not the strain rate.

Preliminary experiments with a rectangular interface showed that the influence of the side walls on the sheet was non-negligible. This is believed to be due to the fact that the particle raft has a non-zero shear modulus. Consequently, the non-slip condition at the side walls is noticeable throughout the sheet. Introducing different strains across the particle raft may alleviate this problem, while also making cascading favorable along the large-to-small strain transition. Thus, the moving wall and the fixed wall opposite to it were each fitted with a block of acrylic, which reduced the length of the interface at the middle of the raft (see Figure 3-1).

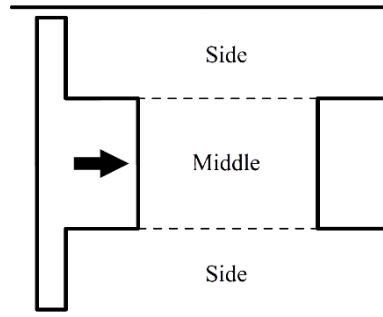


Figure 3-1: Schematic representation of the Langmuir trough.

The particles were spread on a decane-water interface. The decane was manufactured by Sigma-Aldrich (anhydrous, $\geq 99\%$) and the water was deionized at the University of Massachusetts through reverse osmosis. 0.3 ml of solution (0.1 ml of solution of particles in water and 0.2 ml of water and isopropanol at 5:4 volume ratio) were used to deliver the particles to the interface. The solutions of particles in water were made with enough particles to cover the area of the interface at least 5 times in close packing, and were flushed to remove any surfactants that may be extant from the manufacturing process. Flushing was done by adding approximately 1 ml of deionized water to the particle solution, then sonicating the solution for 5 minutes, followed by 5 minutes in a centrifuge at 3500 rpm, and finally removing the extra 1 ml. This process was repeated 3 times for each particle solution except the 0.1 μm particles (because those particles are too small to sink in water) and the lycopodium powder (because it was sprinkled directly onto the interface).

Isopropanol (Fisher Scientific®) was used as a spreading agent due to its miscibility both with water and decane, as in Reynaert, Moldenaers, & Vermant (2006) and Mulligan (2012). Its effects on the results are expected to be small due to the minimal concentration and its high volatility at room temperature.

Since the particle-laden interface is extremely diffusive, directly visualizing the wrinkles under ambient light was difficult. Thus, a nearly horizontal laser (Melles Girot 05-LLP-851, He-Ne) and a cylindrical lens were used to create a light sheet and illuminate the buckled interface. This led to strong contrast between the crests and troughs of the wrinkles, so it was possible to identify each individual wrinkle. A small angle to the

horizontal allowed several wrinkles to be detected, but large angles made the laser hit the entire area of the photograph, which eliminated the contrast. Therefore, the angle of the laser had to be tuned to produce the best possible contrast.

Imaging was done using a CMOS camera (UI-154x by iDS®, 1280x1024 pixels) combined with a long range microscopic lens. Each picture covered about 3.4 x 2.7 mm, which meant they could not cover the entire surface of the Langmuir trough. This problem was solved by placing the Langmuir trough on a moving stage and taking several pictures, which were later combined using image processing software (Image Magick®).

This part of the process is illustrated in Figure 3-2. Steps IV, V and VI may be repeated a number of times depending on the experimental protocol.

The images obtained in step VI were processed in different ways depending on the part of the work that was under study (Figure 3-3). Measurements of average wavelength for the regime transition and the hysteresis data were obtained by measuring a train of waves and dividing the resulting length by the number of wrinkles in the train (Figure 3-3, VII-A), which had been done for ocean waves in Libby, Libby, & Lawrence (1969). The area of the interface that had buckled in a given image (used in the hysteresis section) was measured by manually filling the buckled areas of the image with black and calculating the total area of black on the interface (Figure 3-3, VII-B). Finally, cascading data was obtained by isolating the areas of the interface where changes in wavelength occurred and applying automated image processing to those areas. This was done due to the large number of points that was necessary in that part of the work (Figure 3-3, VII-C).

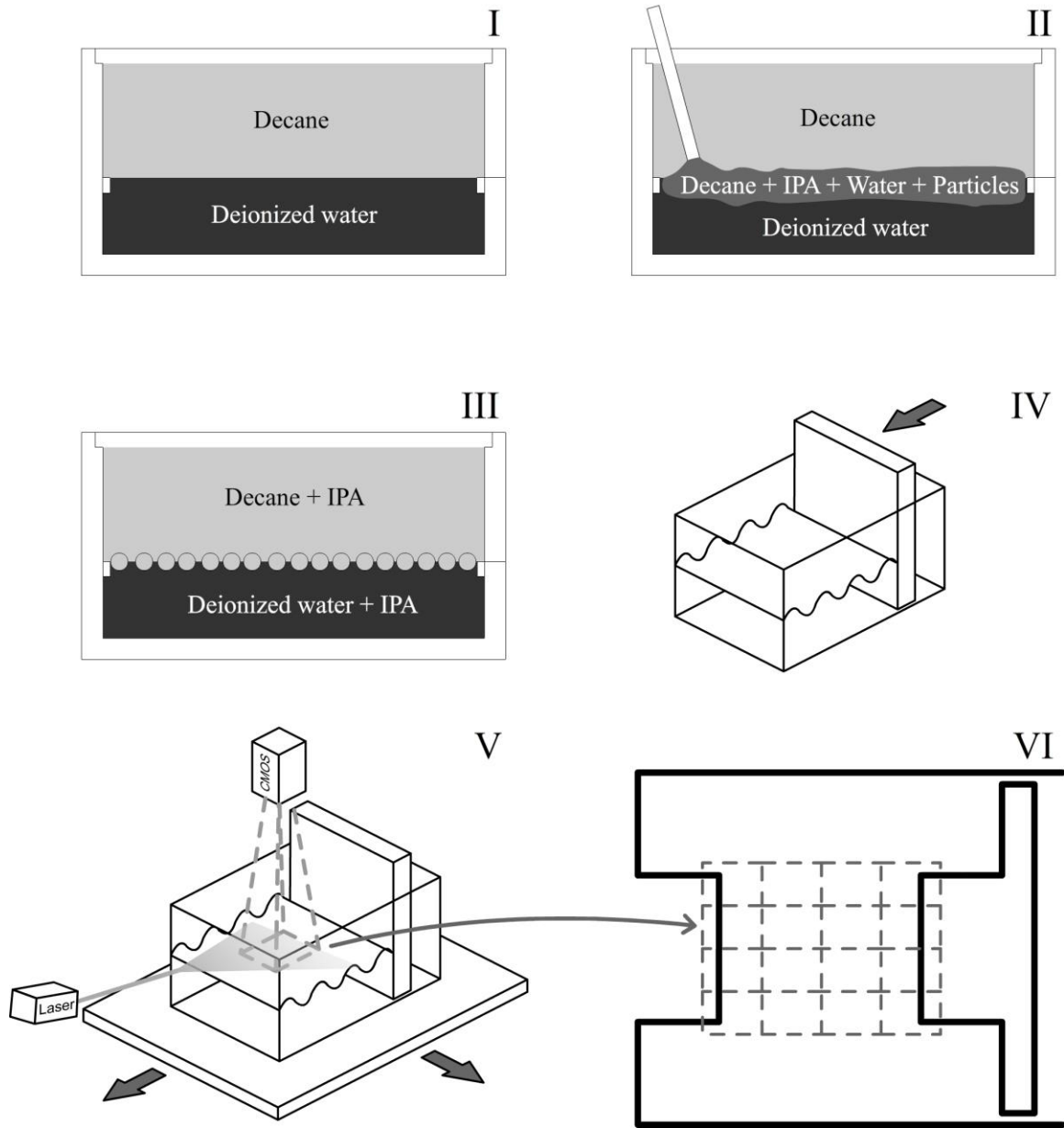
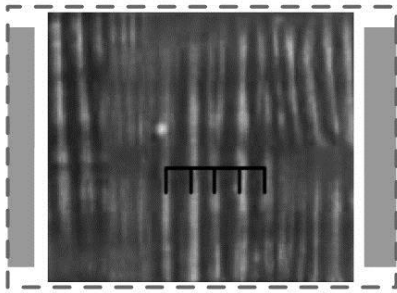
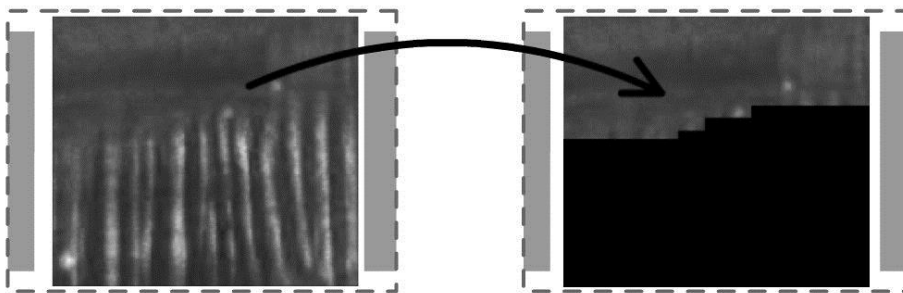


Figure 3-2: Diagram of experimental method. I, II and III) Spreading the particles on the decane-water interface; IV) Compressing the interface with the moving wall; V) Obtaining images using a CMOS camera, a laser and a moving stage; VI) Combining images to form a single picture of the interface.

VII - A: Manual measurement of wavelength



VII - B: Manual measurement of buckled area



VII - C: Automated measurement of wavelength

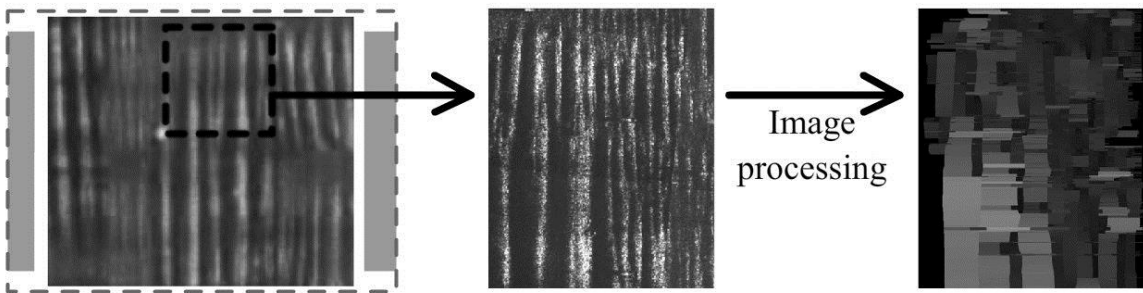


Figure 3-3: Image processing for each part of the present work. A-VII) Hysteresis; B-VII) Measuring wavelength directly for regime transition; C-VII) Cascading.

In order to process the images automatically, they were first enhanced using the “Shadows” effect from ImageJ. “Shadows” applies a specific convolution filter on the image depending on the direction of the shadow. The convolution is done over the surrounding 8 points and the target point, which means the modification is at a much

smaller size-scale than the wavelength of the wrinkles. The resulting images were then interpreted using a purpose-coded C++ console program. The program calculates the distance between subsequent wrinkles horizontally and then applies a correction for the angle of the wrinkles, if necessary (more information on this code can be found in the appendix). The resulting value is the wavelength at that particular point. For details on the program, see Appendix.

Spherical latex particles were used for the experiments; these particles underwent surface treatment during manufacturing in order to become hydrophobic, which allows them to properly attach to the interface. Different diameters were used; the mean diameters and standard deviations were taken as provided by the manufacturer. Lycopodium powder was used as well. The properties of the particles are listed on Table 3-1.

Diameter [mm]	Coefficient of Variation	Material	Manufacturer
0.1	NA	Sulfate latex	Invitrogen®
0.5	2.37%	Polystyrene latex	Polysciences®
0.8	NA	Sulfate latex	Life Technologies®
1	0.98%	Polystyrene latex	Polysciences®
1.8	5.40%	White aliphatic amine latex	Invitrogen®
2.9	4.30%	White sulfate polystyrene latex	Invitrogen®
10	7.69%	Sulfate latex	Invitrogen®
31	7.11%	Lycopodium powder	Carolina®

Table 3-1: Properties of the particles used in the present work.

The latex particles are manufactured in controlled processes and are believed to be spherical to great accuracy. On the other hand, lycopodium particles are naturally occurring and therefore may not be perfectly spherical, as shown in Figure 3-4.

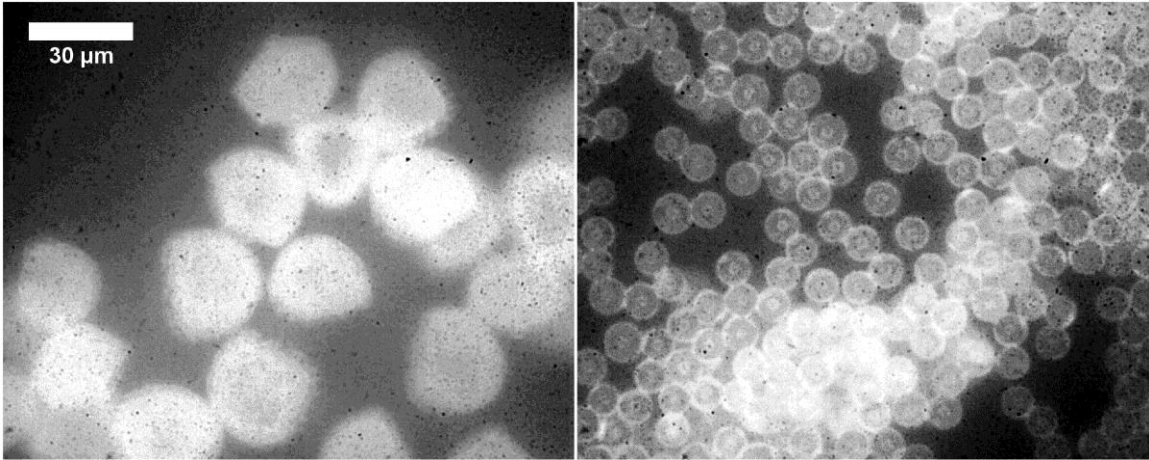


Figure 3-4: Lycopodium powder (left) and 10 μm latex particles (right) under an optical microscope. The latex particles are clearly spherical, while the lycopodium particles are bullet-shaped.

Thus, it is interesting to quantify the shape of the lycopodium particles and how much it deviates from a sphere. While measuring the shape of particles in 3 dimensions is very difficult, an estimate of how spherical they are can be obtained by calculating their circularity in 2 dimensions. Circularity is defined as follows:

$$C = \frac{4\pi A_s}{P_s^2} \quad (3-1)$$

Where A_s is the projected area of the particle and P_s is the perimeter of the projection of the particle. On average, the lycopodium particles have a circularity of 0.94 with a standard deviation of 0.022. Figure 3-5 shows how this value compares to the circularities of a square, a regular octagon and a circle.

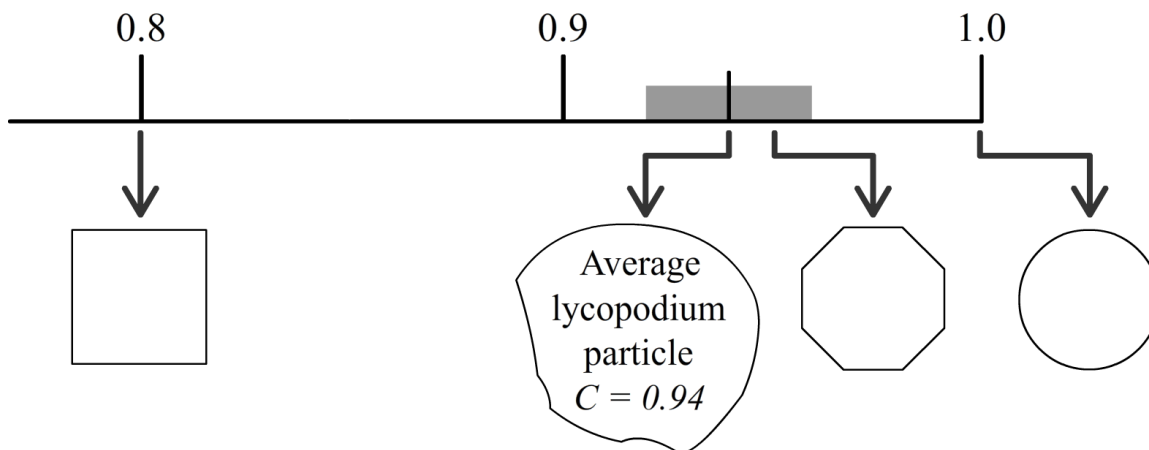


Figure 3-5: Average circularity of lycopodium particles compared to the circularities of a square, a regular octagon and a circle.

Based on this estimate of circularity and assuming that the particles have roughly the same shape if projected on any plane in space, it is reasonable to say that lycopodium particles are nearly spherical in shape.

The Langmuir trough was filled with water to 24 ml, which is 2 ml above the point where the interface is flat. Then, 10 ml of decane were inserted on top of the water. Next, 0.3 ml of particle solution were carefully injected using a syringe. The particles usually adsorbed within a few seconds and viscous effects quickly dampened the flow. At least 1 min was given for these processes to occur. It is important that the interface be flat, otherwise bending is facilitated near the walls, so the extra 2 ml of water were removed before the experimental protocol was initiated.

The protocol consisted of successive compressions of the interface to prescribed strains. Since the Langmuir trough was hand-operated, the strain rate was not controlled; nevertheless, motion was slow in order to avoid strong flows within the trough.

Table 3-2 shows the engineering strain on each part of the trough as a function of the step within the process. Images were taken at every step except those with 0% strain. In the present work, the word “strain” will be used as a synonym for engineering strain unless otherwise specified (e.g. local strain).

Step	Engineering Strain	
	Side	Middle
1	0%	0%
2	8%	15%
3	16%	32%
4	0%	0%
5	16%	32%
6	24%	49%
7	40%	81%
8	0%	0%
9	16%	32%
10	24%	49%
11	40%	81%

Table 3-2: Engineering strain as a function of step.

CHAPTER 4

RESULTS AND DISCUSSION

4.1 Regime transition

In this part of the work, the wavelengths were measured manually by selecting a train of wrinkles and measuring its length, which was then divided by the number of wrinkles in the train. These measurements were verified using Fourier transforms of the images and the purpose-coded C++ program for select cases. The results are shown in Figure 4-1.

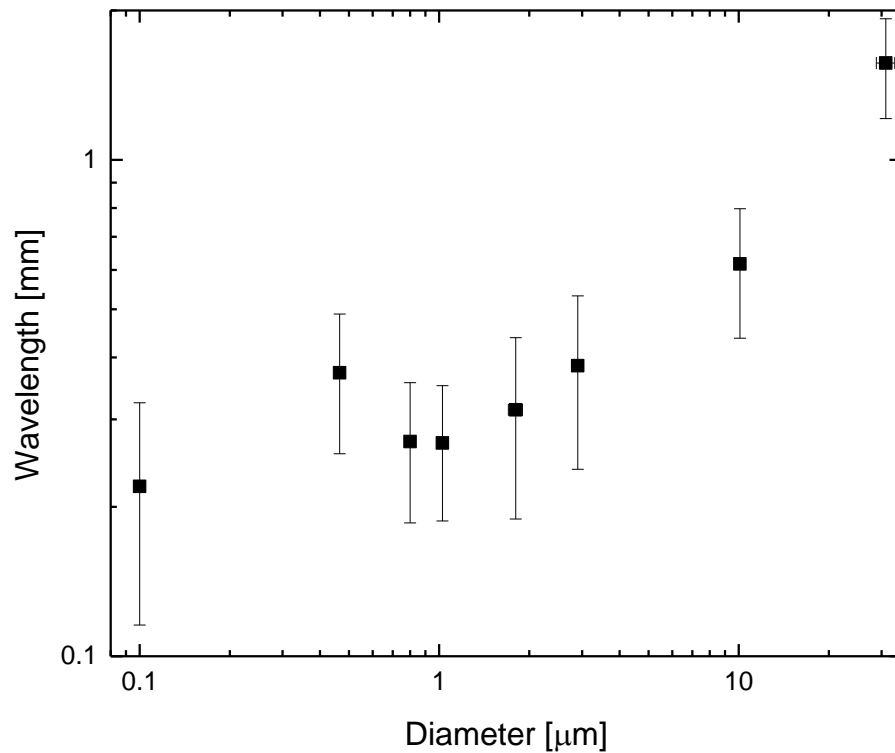


Figure 4-1: Wavelength as a function of diameter.

In Figure 4-1, the squares denote the original data with no adjustments. The points for 0.1 μm and 0.5 μm seem to sit on a separate trend from the other data points, though both trends have similar slope (the data can be made to collapse on a single line after mathematical manipulation which will be discussed shortly). That is remarkable because the theory proposed by Vella et al. (2004) indicates that the wavelength should increase steadily with diameter with an exponent of 0.5. Mathematically,

$$\lambda \propto d^m, m = 0.5 \quad (4-1)$$

This would suggest that all of the data should collapse on a single line of slope 0.5, which is not the case. It should be pointed out that this slope has been recovered for air-water interfaces with particles in the millimeter/sub-millimeter range (Vella et al., 2004), but this has not been done for particles well within the micron range as is the case here. Consequently, a transition in behavior in this range would not have been reported before.

Results from the literature hint at the possibility of a transition in the micron-range. Aveyard, Clint, Nees, & Paunov (2000) showed that sulfate polystyrene latex particles of 1.5 and 2.6 μm in diameter arranged in a different fashion to particles below 0.5 μm -diameter. Monteux, Kirkwood, et al. (2007) reported a clear difference in behavior between 9 μm particles and particles smaller than 2.5 μm (both polystyrene latex), where the latter form hexagonal lattices while the former aggregate on a fractal network due to stronger capillary interaction. That leads to the possibility of a transition due to different packing regimes. Yet, this explanation is unlikely to be the reason behind this difference in behavior. For example, lycopodium particles (diameter: 31 μm) on an air-water interface are certainly in the range where gravity becomes relevant (Figure 1-3c), forming fractal structures when uncompressed as Figure 4-2 shows.

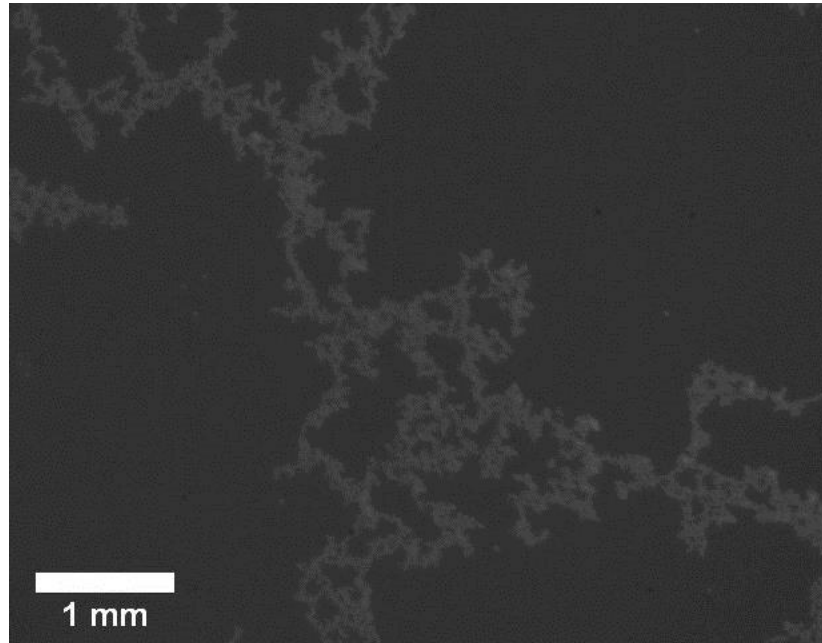


Figure 4-2: Fractal formation of lycopodium particles on an air-water interface.

However, when compressed to the point of buckling, these particles are very closely packed (Figure 4-3).

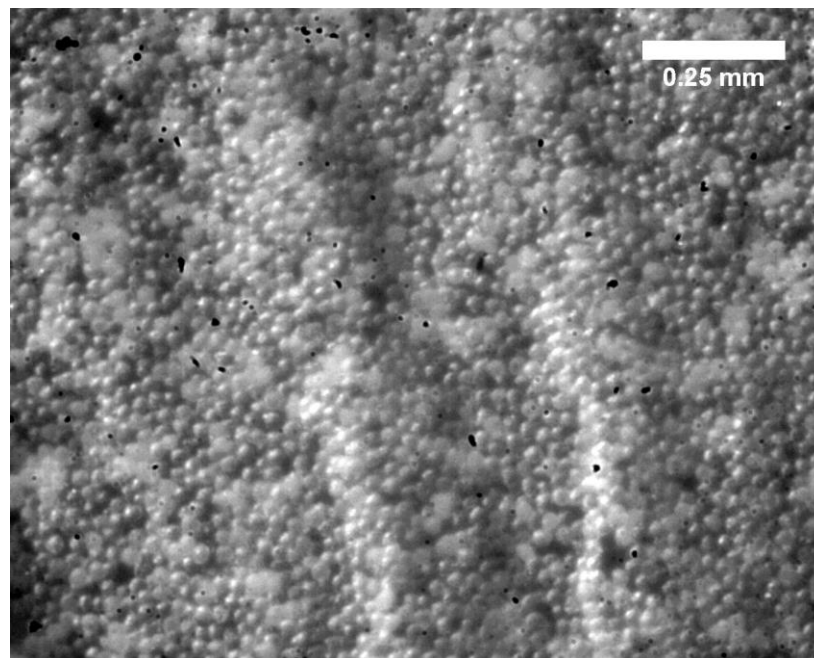


Figure 4-3: Lycopodium particles on a buckled air-water interface.

Therefore, the packing regime is unlikely to change to any relevant degree as the diameter is changed, so this is not a likely explanation for the transition.

Another possible explanation comes from work by Helseth, Muruganathan, Zhang, & Fischer (2005) on ring-like solid deposits left behind upon drying particle-coated droplets. The results presented in that work indicate that Brownian motion is noticeably more pronounced for 0.5 μm than for 1.4 μm particles. This could increase the effective area that each particle occupies, therefore changing both the effective diameter and the solid coverage ratio of the interface. However, even if more pronounced for smaller particles, Brownian motion in 2 dimensions tends to be near negligible, so this is also an unlikely explanation.

Alternatively, the transition could be due to the formation of multilayers. Leahy et al. (2010) showed that this occurs for 6 nm gold particles at an air-liquid interface, with the formation of trilayers. This would lead to a larger bending stiffness, which would explain the increase in wavelength.

Indeed, some irreversible stacking of layers of interface has been observed for 0.1 μm particles, as Figure 4-4, step 9 shows. In the figure, steps 5 (32% strain), 7 (81% strain) and 9 (32% strain) are depicted. At step 5, the interface is completely flat. Compression to step 7 leads to widespread buckling. Then, stacks seem to remain through step 9. It is impossible to determine the nature of the stacks (bilayer, trilayer, etc.) from this data because of the smallness of the buckling features.

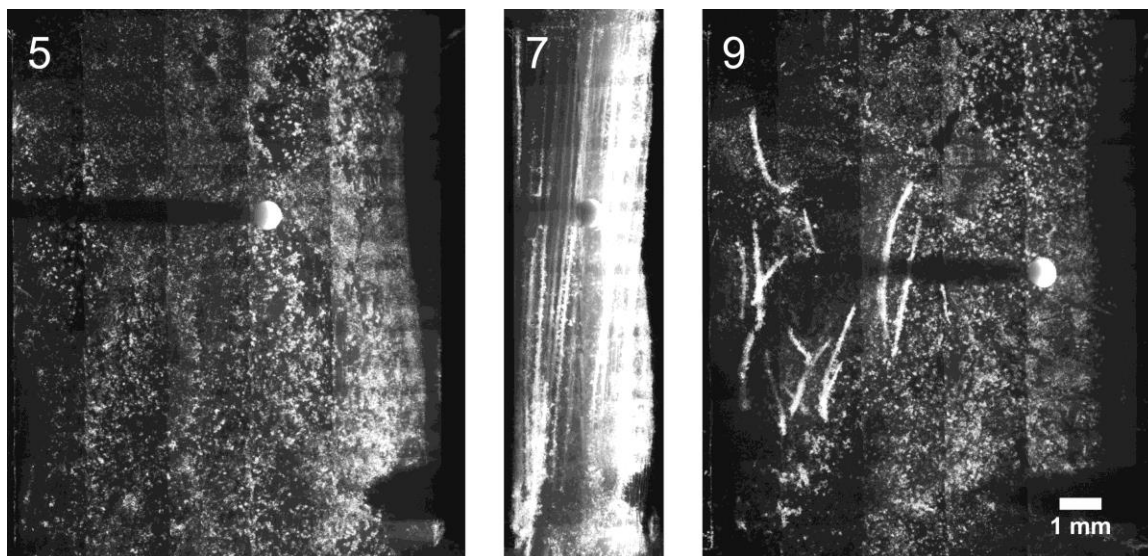


Figure 4-4: 0.1 μm -particle raft under compression. At step 5 (32% strain), the interface is flat. It is compressed to step 7 (81% strain), where buckling is widespread. Then, the interface is stretched to step 8 (0% strain) and back to step 9 (32% strain). At step 9, stacks of particles can be observed as bright stripes approximately perpendicular to the direction of compression.

On the other hand, the reversible formation of trilayers has been observed in lycopodium rafts on air-water interfaces (e.g. Figure 4-5). In the case of lycopodium, these trilayers only formed after very substantial compression (with the area of the trough approaching zero) was applied to the interface. That is, the formation of trilayers in lycopodium rafts follows a different process than that observed in the sub-micron range. In the former, wrinkles only collapse under extreme global strain (almost 100%), while in the latter they could occur at much smaller strains. Because the largest strain in the experimental protocol is about 80%, trilayers are not expected to have occurred for diameters at and above 1 μm . Still, inducing trilayers on lycopodium rafts allows for optical online observation of a trilayer, which is impossible for small particles, which makes it

useful as an illustration for the purposes of this explanation. In order to avoid confusion, an elucidation of the different kinds of trilayer formation follows.

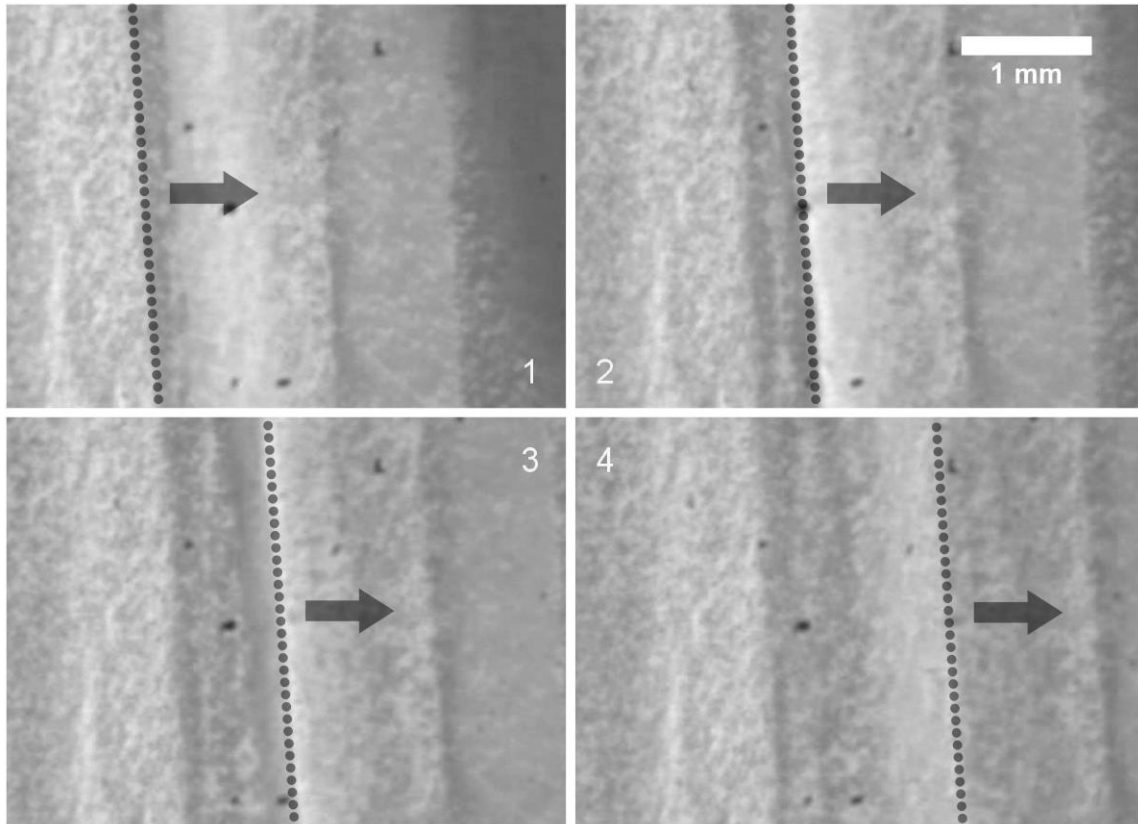


Figure 4-5: Trilayer unfolding upon release of compression. Lycopodium on an air-water interface.

For most particle-laden interfaces in the range presented here ($0.5 \mu\text{m}$ to $31 \mu\text{m}$), the first wrinkles are observed in the vicinity of the moving wall, such as in Figure 4-6a (left-hand side).

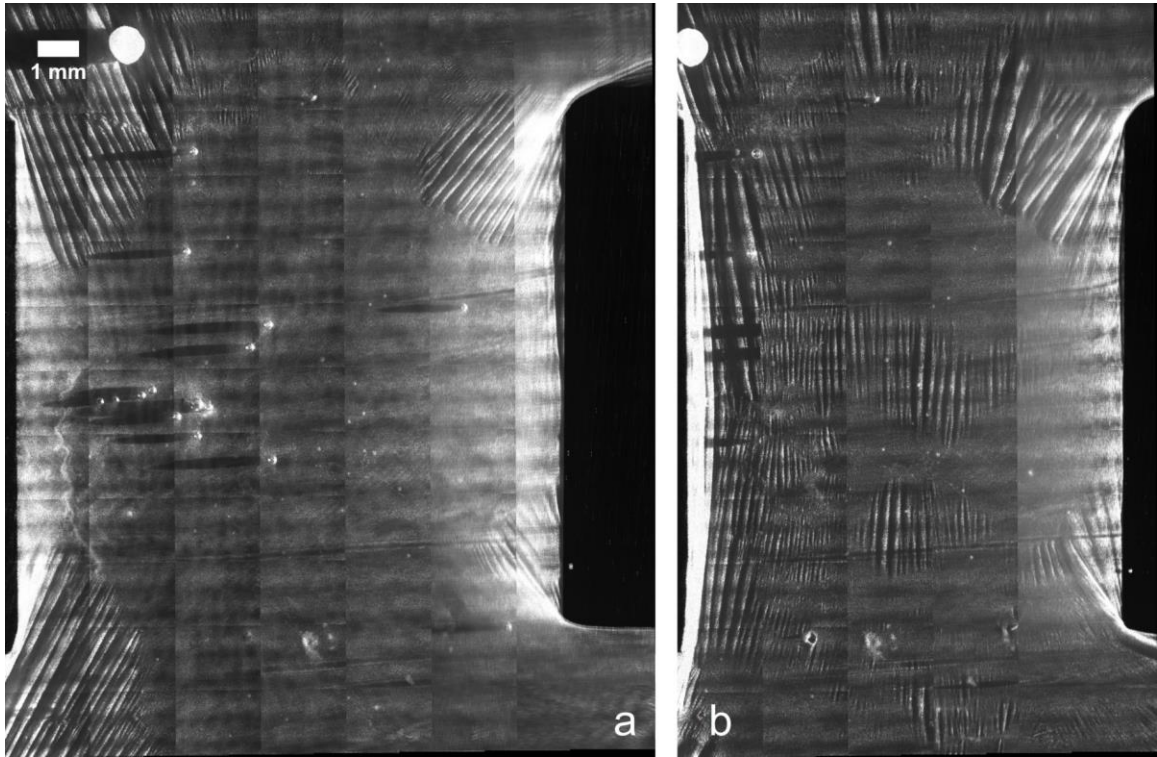


Figure 4-6: Buckling of a 1.8- μm -particle raft: a) Wrinkling starts near the moving wall, with shear from the side walls; b) Folds form near the moving wall, wrinkles develop in the middle of the sheet, where shear seems less pronounced.

This happens because of the shear on the side walls, which effectively compresses the part of the interface that is close to the moving wall. This is evidenced by the fact that the wrinkles in Figure 4-6a are not completely aligned with the direction of compression, instead pointing slightly towards the sides of the trough.

When the interface is compressed further, these first wrinkles tend to develop into folds, such as the ones observed on the left-hand side of Figure 4-6b (the folds appear as a particularly bright area next to the moving wall). This occurs because it is energetically cheaper to bend an object past the onset of buckling than it is to induce buckling in other

parts of the object (recall that in Figure 1-6 the energy is localized into a fold once the straw is compressed beyond the onset of buckling).

Once the folds develop, they do not collapse upon themselves to form a trilayer, but rather remain upright, probably because the bending stiffness of the combined layers is too large to allow for a collapse of the base of the fold. As a result, the folds effectively cease to play a role in the subsequent buckling of the interface, simply accumulating near the moving wall. On the other hand, smaller particles are believed to lead to a smaller bending stiffness, so it is possible that trilayers could form in that case. Figure 4-7 is a schematic of these two possibilities.

The case represented in Figure 4-7d is more likely to occur in lycopodium sheets on air-water interfaces, which have high bending stiffness. However, if compressed very substantially (approaching 100% strain), the folds will eventually collapse, leading to the trilayers observed in Figure 4-5. Very high strains were purposely induced on a lycopodium sheet to demonstrate trilayers at a scale that could be detected with regular optical equipment, thus allowing Figure 4-5 to be obtained. Such high strains were never induced during the experimental protocol, so trilayers are not believed to have formed through collapse of folds that is associated with rafts of high bending stiffness. Rather, they can only have formed directly through the process shown in Figure 4-7b and Figure 4-7c, which requires low bending stiffness.

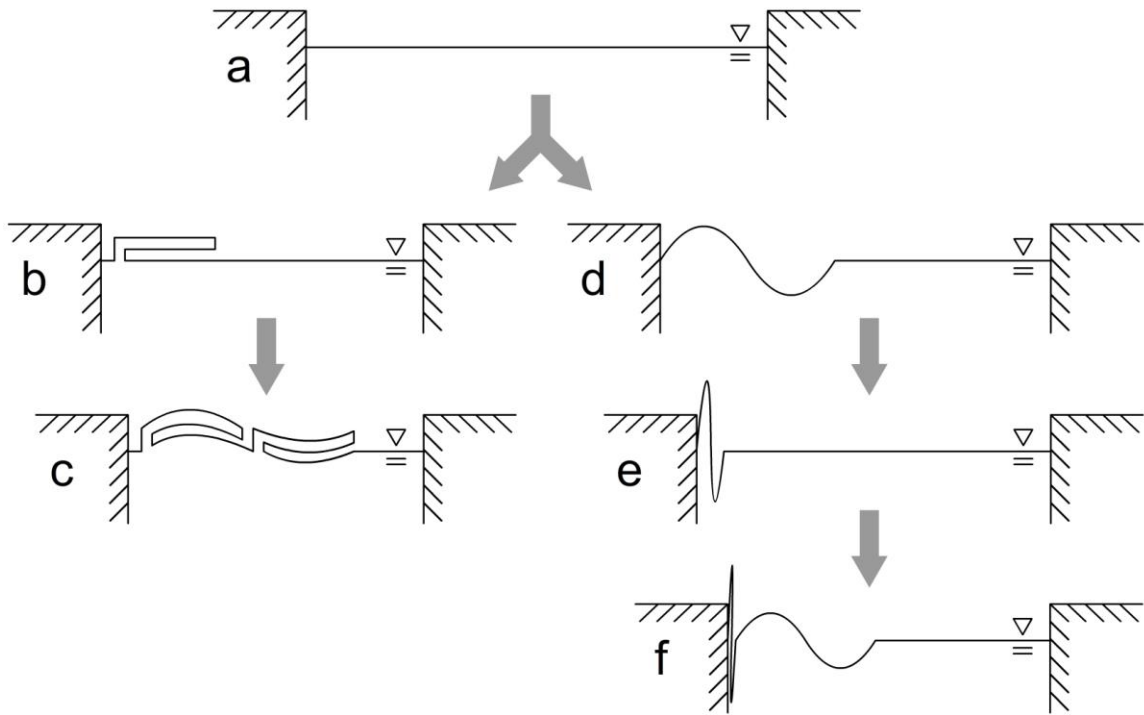


Figure 4-7: Schematic of the development of folds: a) An interface populated with particles (not shown) before compression; b) If the bending stiffness is low, the interface folds upon itself, forming a trilayer; c) Trilayers subsequently buckle at a higher wavelength; d) If the bending stiffness is high, a wrinkle develops and no trilayers form; e) Further compression leads to folding near the moving wall; f) New wrinkles form beyond the fold.

Therefore, it is possible that trilayers formed only for the rafts of particles in the sub-micron range. That leads to the question of what would be the buckling wavelength of a trilayer. A simple modification to the theory proposed by Vella et al. (2004) can offer an estimate of the behavior of a particle-laden interface in the case of buckling of trilayers (buckling after the condition depicted in Figure 4-7c). The expression for wrinkling wavelength proposed in that work is:

$$\lambda = \pi \left[\frac{4}{3(1-\varphi)(1-\nu)} \right]^{1/4} \left(\frac{t^3}{d} \right)^{1/4} L_c^{1/2} \quad (4-2)$$

where φ is the solid area ratio of the interface, ν is the Poisson ratio, t is the thickness of the interface, d is the diameter of the particles and L_c is the capillary length. Then, a trilayer can be said to behave approximately as a single layer with an “effective” diameter calculated by the expression below:

$$d_{eff} = n^{3/2} d \quad (4-3)$$

where n is the number of layers in the stack and is generally expected to be an odd number. For a trilayer, this yields:

$$d_{eff} \cong 5.196d \quad (4-4)$$

That is, a particle raft that has buckled into a trilayer is expected to behave like a raft of particles of larger diameter (about 5 times the original diameter). Since the formation of trilayers requires that part of the interface buckle as a monolayer beforehand, it should be expected that a smaller wavelength be detected before the trilayers form. Figure 4-8 shows the wavelength as a function of step for the two cases where trilayers are believed to have influenced the results in Figure 4-1, 0.1 μm and 0.5 μm .

Step 2 corresponds to 15% engineering strain, which is the lowest strain for which wavelength data was obtained. Thus, it is interesting that the wavelength is particularly low at this step on the 0.5 μm case. This indicates that trilayers may not have formed yet at this strain, leading to a very low wavelength. This is supported by the fact that the point at step 2 (15% strain) collapses with the remaining data (where trilayers are not expected) while the average over all steps does not (see Figure 4-9). Note that the other point with small wavelength (step 7) corresponds to very high engineering strain (81%), so the small

wavelength could be a result of widespread folding of the interface at that point. Note also that step 9 is at 15% engineering strain, but the wavelength is much larger than on step 2, which is also at 15% strain; this indicates that once trilayers were induced in the first compression cycle, it may become easier to induce them in subsequent compression cycles, even at smaller global strains depending on the local strains on the raft.

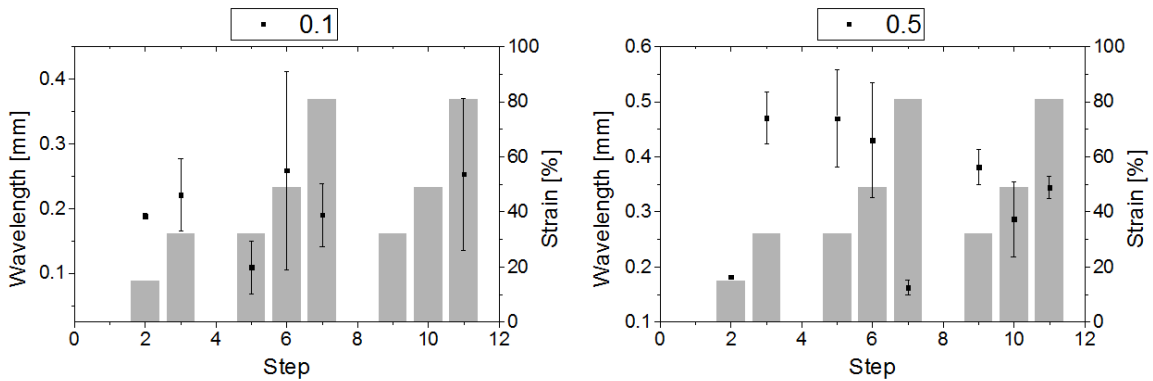


Figure 4-8: Wavelength as a function of step in experimental protocol (see Table 3-2 for corresponding strain), for the 0.1 μm and 0.5 μm cases.

Considering the exposed above, it can be said that there is evidence that trilayers do form on the 0.5 μm case. This is not as clear for the 0.1 μm case. At step 2, the measured wavelength is reduced, but not by enough to fit the trendline. This may be because although the global strain is small, the particle distribution is not uniform and the strain can become localized. As a result, very little of the interface is observed to buckle. As will be addressed later, successive compressions can rearrange and realign particles on the interface to make the raft more homogeneously packed and the imposed strains more uniform. Thus although the engineering strain at step 5 is larger than step 2 (32% and 15%, respectively), the fraction of the surface buckling is significantly larger and the local strain may be in fact much less. The wavelength measured at step 5 for 0.1 μm particle rafts is also significantly

smaller than at larger strains and again fits the Vella et al. predictions for a monolayer of particles very well.

By applying equation (4-4) for effective diameter on the data points at 0.1 μm and 0.5 μm , the data points denoted by triangles in Figure 4-9 are obtained. It is clear that the data collapses within the same power law. This supports the explanation that a transition between regimes occurs at the micron range and that this transition is given by a shift in the mechanism of buckling, with the formation of trilayers below the transition.

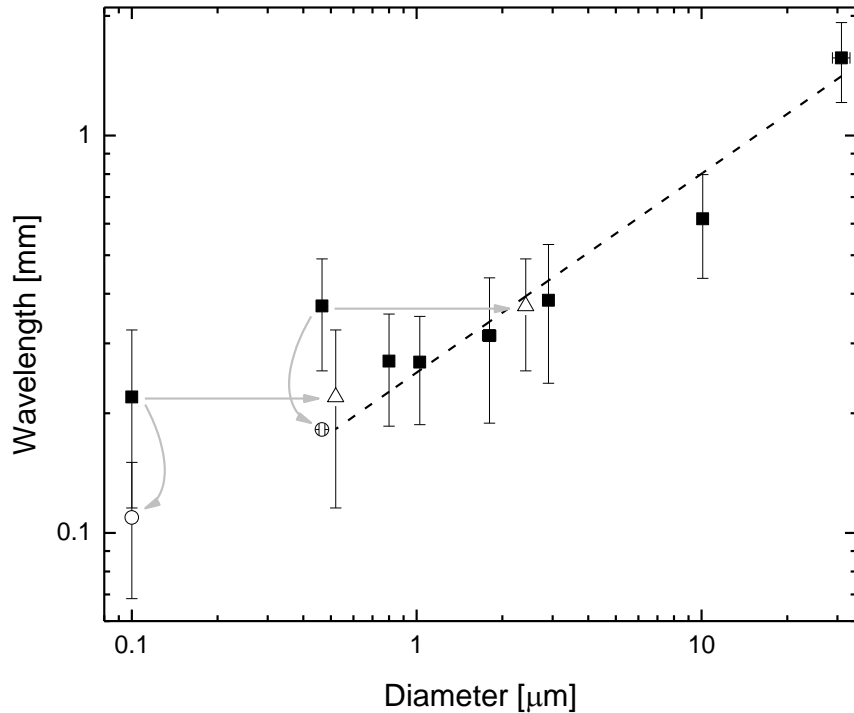


Figure 4-9: Wavelength as a function of diameter. Squares show original data, triangles show data for 0.1 μm and 0.5 μm after the diameter shift. The dashed line is a fit with exponent 0.5 over the adjusted data ($r^2=0.73$). The circles represent step 5 (32% strain) for 0.1 μm and step 2 (15% strain) for 0.5 μm .

The dashed line in Figure 4-9 shows a fit with exponent 0.5, i.e. that predicted by Vella et al. (2004). The data collapses well within the experimental error, and the coefficient of determination is 0.73. This is remarkable because it shows that the theory holds well for a decane-water interface in this diameter range. Thus, these results support the theory proposed by Vella et al. (2004) as a way to describe the wavelength of buckling of particle-laden fluid-liquid interfaces.

Furthermore, the hypothesis of the formation of trilayers leads to a full data collapse on the trend predicted by theory. Thus, the adaptation presented here is a viable option to predicting the behavior of particle-laden interfaces below the micron range, provided enough compression is imposed for trilayers to form in the first place.

Finally, two conclusions are proposed based on the data presented here. First, there is a transition in the behavior of particle-laden interfaces in the micron-range and this transition is believed to be caused by the formation of trilayers on interfaces populated by small particles (below the transition diameter). This adaptation leads to a full data collapse, supporting this as a model of the behavior of particle-laden interfaces below the transition. Second, the trend proposed in existing theory is acceptable within experimental error, which extends its known range of applicability to decane-water interfaces.

4.2 Cascading and branching

Areas of different wavelength often occur on the same particle raft (see example in Figure 4-10). In those cases, the interface must deform in such a way as to accommodate both wavelengths, as has been shown to be the case with thin solid sheets, for example in Vandeparre et al. (2011) and Huang et al. (2010).

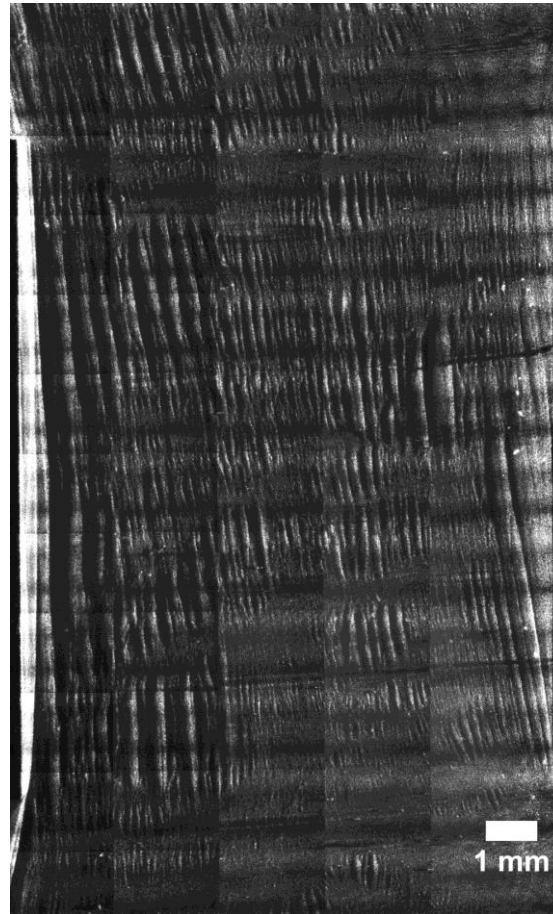


Figure 4-10: a 0.5- μm -particle raft under compression. Note that wrinkles occur in different wavelengths at different parts of the raft.

This transition has been observed to occur in a number of different ways:

- a) One wrinkle splits into two wrinkles. This usually occurs in the middle of a buckled area. Transitions from one to two wrinkles have been proposed to be the building block of the global transition between wavelengths (Vandeparre et al., 2011). Thus, this kind of transition does not differ fundamentally from what is observed in thin solid sheets.
- b) A wrinkle simply ends at the edge of a buckled area, without any transition to a smaller wavelength. This often happens in areas where other wrinkles split

into smaller wavelengths, which suggests that some stress is released. Since the wavelength at the edge of the buckled area – or, equivalently, at the edge of a thin solid sheet - is a function of the stress state in that region, the fact that wrinkles can end abruptly does not mean that the particle-laden interface behaves in any way differently from thin solid sheets.

- c) One wrinkle splits into between three and six short wrinkles. This usually occurs at the edges of buckled areas. This has not been reported for thin solid sheets, so it is likely limited to particle-laden interfaces.
- d) A flat area develops between the two wavelengths that are to be connected. This seems to occur when two areas that were previously buckled are pushed together due to compression, nearly (but not completely) eliminating the flat area between them. This is also particular to particle-laden interfaces.
- e) A sharp fault-like transition develops. This is characterized by a discontinuity in wavelength and possible rupture of the particle raft. This may indicate discontinuities in packing and has not been reported for thin solid sheets.
- f) The wavelength transitions gradually from one value to the other.

Figure 4-11 shows examples of each of those transitions.

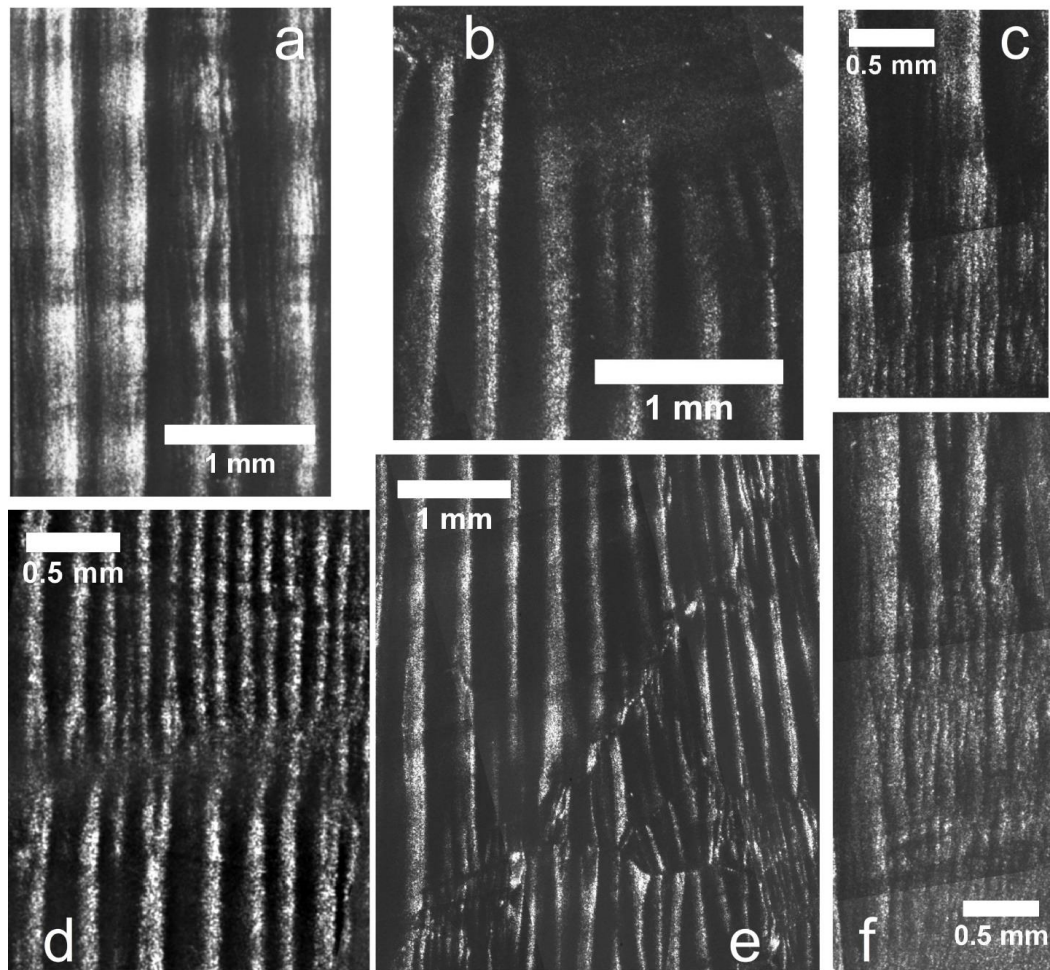


Figure 4-11: Wavelength transition events in particle-laden interfaces: a) A wrinkle splits into two wrinkles, 1.8-micron-particle raft; b) Wrinkles end abruptly at the end of a buckled area, while other wrinkles split before ending, 0.8-micron-particle raft; c) A wrinkle splits into five wrinkles at the edge of a buckled area, 0.5-micron-particle raft; d) The transition between the wrinkles at the top and bottom occurs through a flat area, 1.0-micron-particle raft; e) Fault-like transition on a 0.8-micron-particle raft; f) Gradual transition from a large wavelength to a much smaller wavelength, then a sudden transition to flat, 2.9-micron-particle raft.

Cases *c-e* have never been reported for the analogous phenomenon of cascading on thin solid sheets, particularly the split into many wrinkles shown in Figure 4-11c. These are presented here as new observations. Cases *a* and *b* can be considered part of cascading as reported for thin solid sheets.

On the other hand, case *f* is characterized by an apparently continuous transition between wavelengths similar to the cascading observed in thin solid sheets. Therefore, it is interesting to compare instances of case *f* in particle-laden interfaces with the theoretical predictions for thin solid sheets.

The smoothness of the transition between wavelengths can be measured by calculating the average wavelength (λ_{avg}) over a line parallel to the edge of the sheet as a function of the distance (y) from that line to the edge of the sheet, as in Vandeparre et al. (2011). An equivalent approach would be to work with the average wave number, as in Huang et al. (2010).

According to the prediction of Vandeparre et al. (2011), the scaling for wavelength with distance from the edge of the sheet should be:

$$\lambda_{light} \propto y^{2/3} \quad (4-5)$$

$$\lambda_{heavy} \propto y^{1/2} \quad (4-6)$$

where “light” refers to sheets under negligible tension in the direction of the wrinkles (perpendicular to the direction of compression) and “heavy” refers to sheets under considerable tension. For example, a thin polymer sheet on a water-fluid interface would be a “heavy” sheet due to the effects of surface tension along the edges of the sheet, as shown in Huang et al. (2010).

It should be pointed out that cascading is, at the most basic level, the collection of several different divisions of wrinkles into two wrinkles of smaller wavelength. Consequently, the continuous trends expected in the theory could only be obtained if a sheet or raft of infinite width were to be measured. For real data measured from a finite particle raft, discontinuities in the average wavelength are to be expected. This is an important issue because the regions of cascading tend to be small in particle-laden interfaces.

Measuring wavelength as a function of the distance from the edge of a particle raft can be technically challenging when compared to the equivalent measurement on a solid sheet, because particle rafts usually do not have a clearly defined edge. On the other hand, it is possible to find flat areas along the interface. The nature of these areas and the reason why they are flat cannot be easily inferred; they could be an area of low particle population, where the effective surface tension is higher, or they could be fully packed but at a different stress-strain state. Results with lycopodium particles on an air-water interface suggest that the difference in packing between a flat area and a buckled area is small (Figure 4-12).

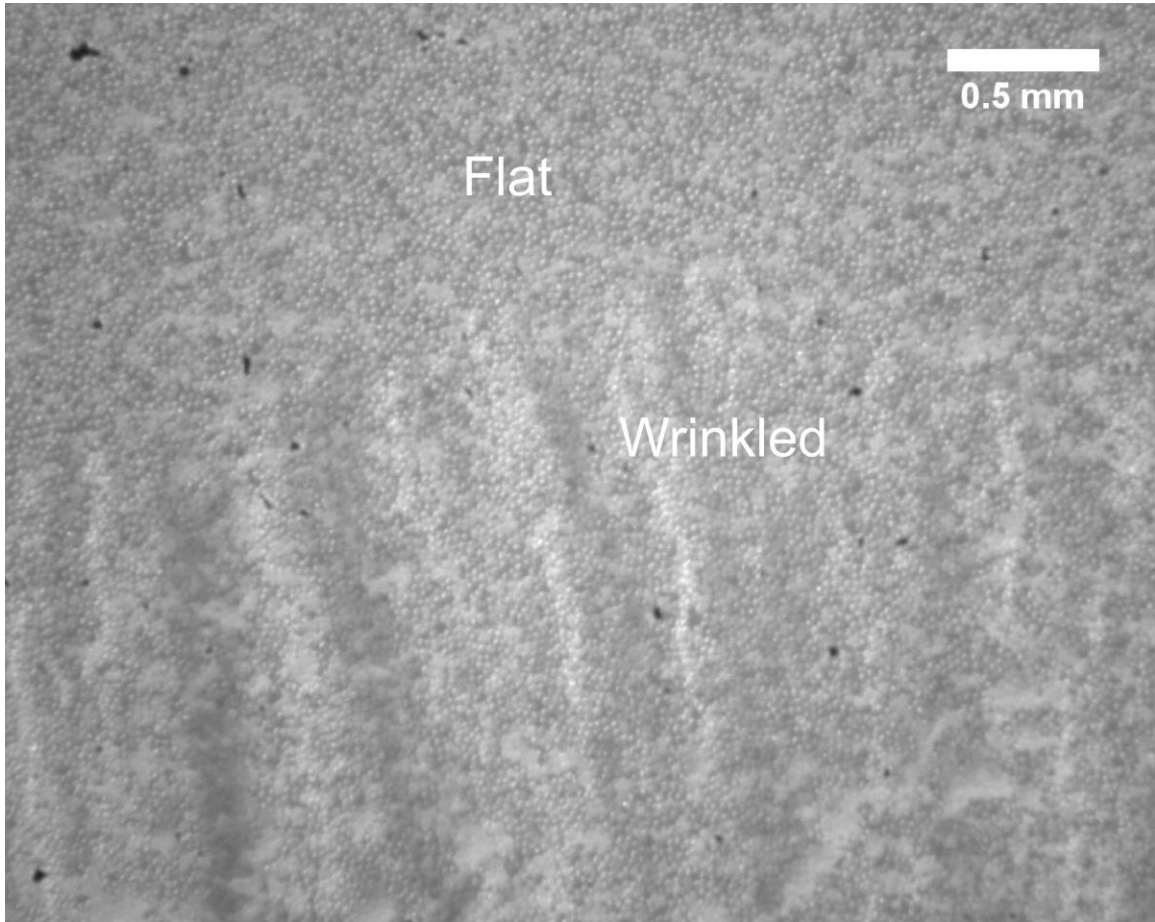


Figure 4-12: Edge of a wrinkled region on an air-water interface populated by lycopodium particles.

Because of the varied nature of these measurements in conditions that are difficult to control, a large amount of data is necessary to obtain reliable results. This leads to the need for elaborate methods of data analysis. For smooth, cascading transitions, the wavelength as a function of the distance to the adjacent flat area was calculated through image processing (see appendix for details on the image processing code). Figure 4-13 shows an example of cascading with the corresponding image processing output.

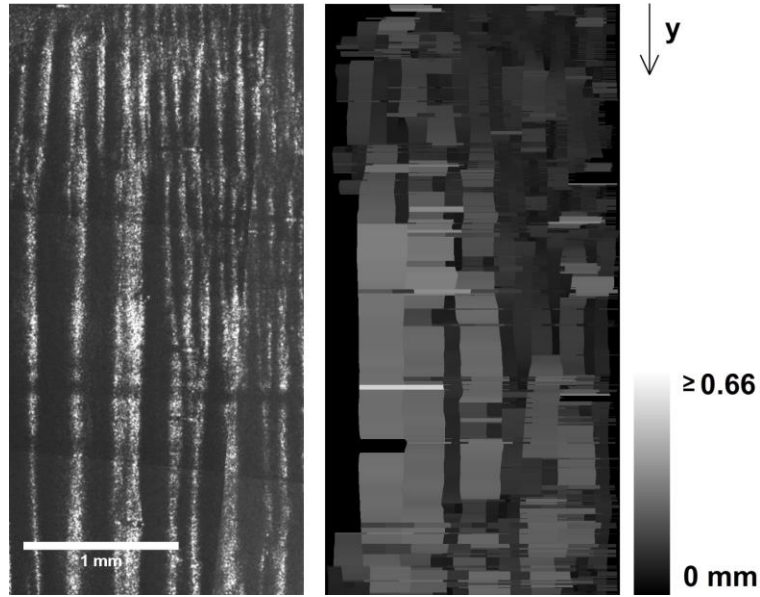


Figure 4-13: Example of cascading (left) and corresponding image processing output (right, wavelengths in grayscale code) on a 1.025 μm particle raft.

A number of wavelengths is obtained for each distance, so they are averaged to yield a function of the form:

$$\lambda_{avg} = f(y) \quad (4-7)$$

where y is the distance from the flat area and λ_{avg} is the average wavelength. The result is a function λ_{avg} for each cascading event. The wavelengths at each y -coordinate are averaged to obtain the average wavelength.

Then, each cascading event was analyzed individually. This was done by obtaining the scaling for each event after subtracting the minimum wavelength for that particular event. In other words, all wavelength-to- y curves were set to start at approximately zero; this removed the influence of the sudden increase in wavelength from the flat area to the buckled area. Mathematically, the wavelength was assumed to be of the form:

$$\lambda = \lambda_{min} + ay^m \quad (4-8)$$

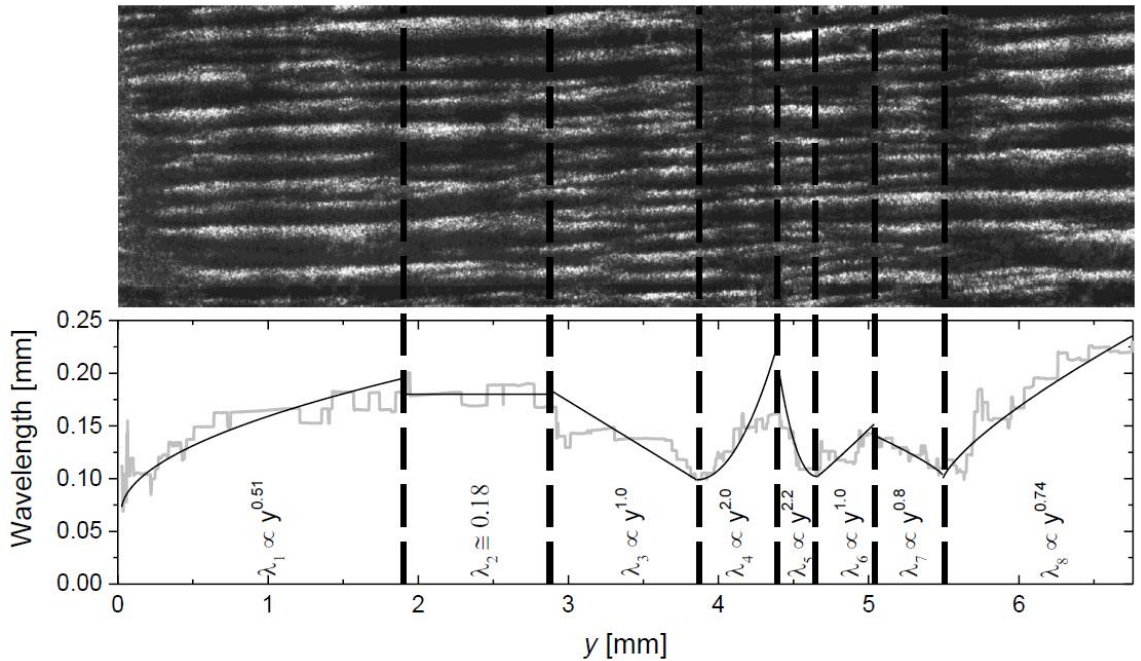


Figure 4-14: The buckled section of a particle raft divided into different transition events (top), and the wavelength as a function of the distance perpendicular to compression (bottom) with power law fits. Events: 1 – smooth (“heavy sheet”) cascading; 2 – constant wavelength; 3, 4, 5, 6 and 7 – sharp transitions; 8 – sharp (“light sheet”) cascading.

Figure 4-14 illustrates how a buckled particle raft may be divided into different wavelength transition events. In the figure, each separate is labeled by a number from 1 to 8. Note that event 1 is next to a flat area of the interface and the wavelength scales with 0.5, indicating that this raft is under tension toward the flat areas. On the other hand, event 8 is surrounded by wrinkles on both sides and the wavelength scales with 0.74, which may indicate compressive forces pushing away from the (very distant) flat area. It should be considered, however, that this exponent is very high compared to the expected $2/3$. The existence of events such as 2 and 3 led to the wide distribution in the histogram (Figure

4-15 below). Events 4, 5, 6 and 7 are particularly short and cannot be considered to characterize cascading.

Applying a fit such as equation (4-8) to each instance of case f (i.e. cascading) that was identified led to the histogram for m shown in Figure 4-15. Note that Figure 4-15 shows the distribution of the exponent m for all the cases of continuous cascading found in the present work.

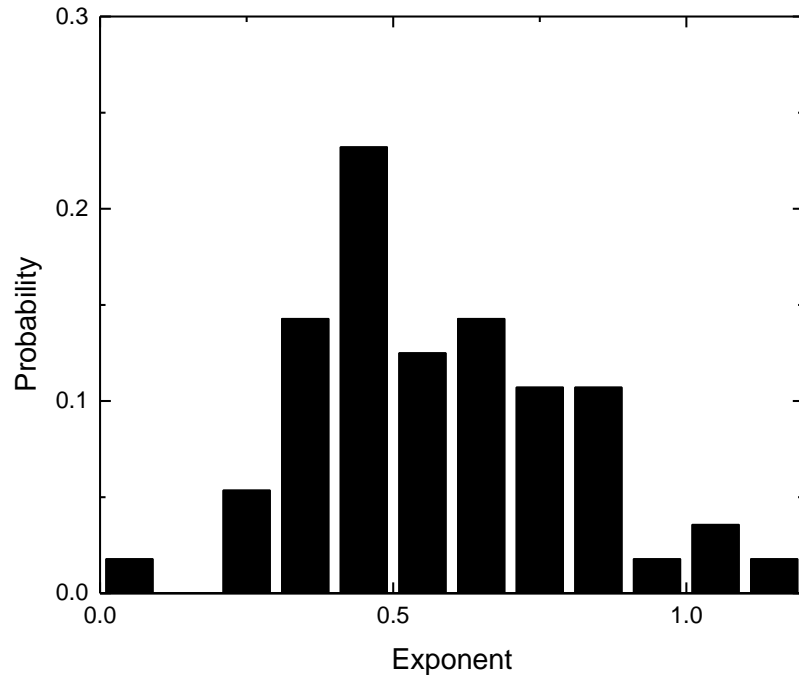


Figure 4-15: Histogram of exponent m for all cascading events recorded.

The mean for this distribution is approximately 0.474, with standard deviation of 0.219 (i.e. the coefficient of variation is about 46.3%). The mode is at 0.4 and the median at 0.439. This indicates a slightly skewed distribution, but all of these values compare favorably with the value of 0.5 for “heavy” sheets proposed by Leahy et al. (2010). Furthermore, the relatively wide tail on the right side indicates the occurrence of occasional

“light” sheet behavior as well. Therefore, it is clear that in general terms the cascading in solid sheets and in particle rafts is similar.

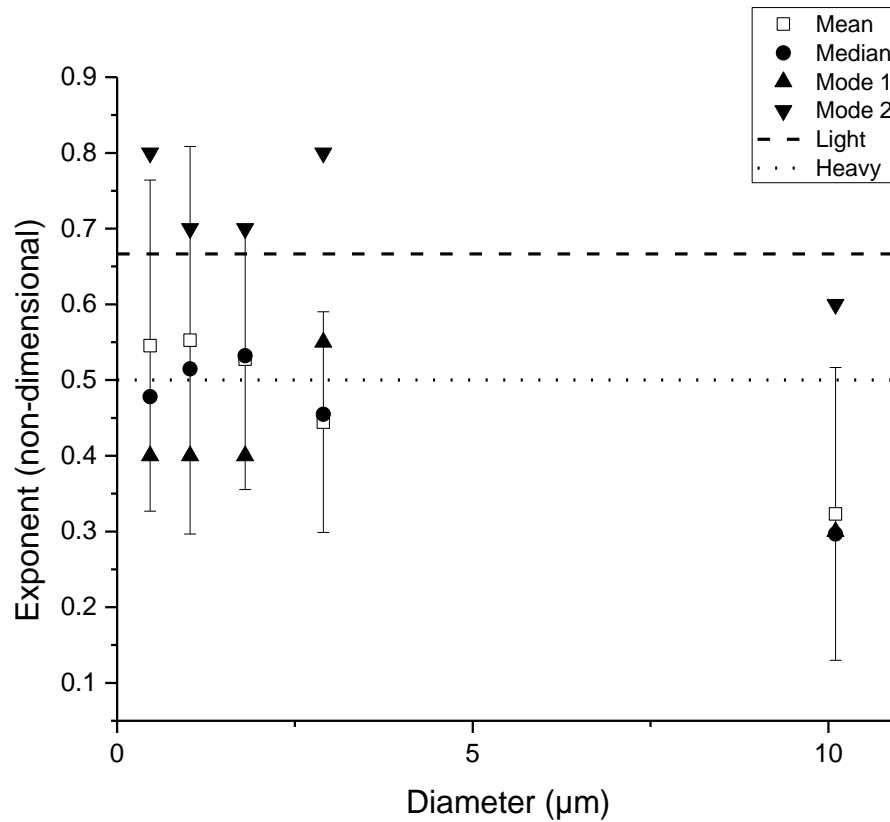


Figure 4-16: Statistics for exponent m as functions of particle diameter.

Figure 4-16 shows the statistics for exponent m as functions of particle diameter. Note that there is a tendency to decreasing exponent as the diameter goes from 2.9 to 10 μm . That tendency is not as clear for diameters smaller than 2.9 μm . Still, the changes are small and the general trend seems to be for two modes, one at the “light” sheet range and another at the “heavy” sheet range, while the skew puts median and mean in the “heavy” sheet range.

Thus, it can be said that the cascading of particle-laden interfaces can be similar to that of thin solid sheets, in that the wavelength transition can be smooth (“heavy sheet behavior” – under lateral tension) or sharp (“light sheet behavior” – no lateral tension). Furthermore, it is clear that most often this transition is smooth. Other exponents that indicate neither kind of behavior are also obtained, most likely due to numerical error due to the use of relatively small data sets.

Still, the wavelength transitions in particle-laden interfaces are not limited to solid-like behavior, as previously shown here (Figure 4-11). Thus, a fundamental difference in behavior from solid sheets has been demonstrated. This points to a novel direction of research into the mechanisms that allow such varied behavior and why these mechanisms are not present elsewhere.

To sum up, in this part of the work it was shown that different wavelengths can occur on a buckled particle-laden interface and that the transition between these wavelengths can occur in a number of ways. More specifically, the transition can occur in manners that are analogous to thin solid sheets (“heavy” and “light” sheet behavior), or in completely novel ways.

4.3 Hysteresis

In general, the internal structure of a solid can only be modified with very high energy input. This occurs because the intermolecular bonds in solids are very strong. Even at the onset of buckling, the energy input is usually too small to cause changes to the

molecular configuration, which means the internal structure remains effectively unchanged.

On the other hand, particles on interfaces are bound by much weaker forces, which are given by the interplay between electrostatic and capillary effects. Consequently, the energy input that is necessary to promote changes in structure is smaller. This is particularly true for interfaces below optimum packing. Therefore, some change in behavior through successive compression cycles should be expected. Figure 4-17 shows an example of the effects of hysteresis.

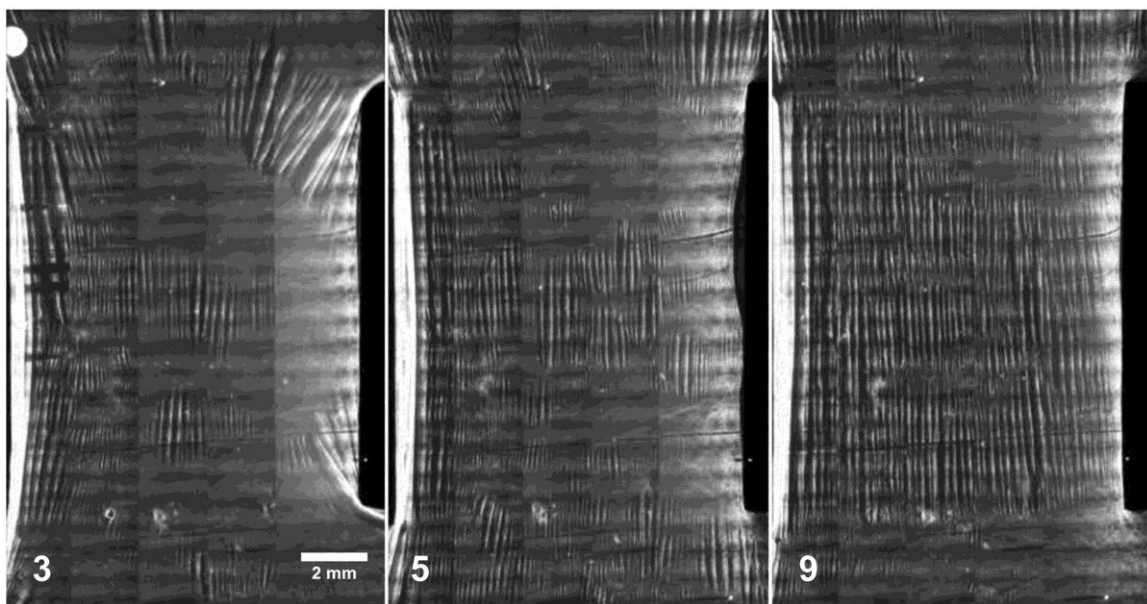


Figure 4-17: Hysteresis on a 1.8 μm -particle raft, numbers represent step in protocol (all at 32% strain).

The changes in behavior between each step are very noticeable. In this case, it seems like there are more particles on the interface at step 9 (32% strain), which would lead to more buckling to cover the same length. That is not always the case, however, as in certain instances buckling actually diminishes through successive compression. Also, it

should be pointed out that the path along the strain axis is different between steps 3 and 5, and steps 5 and 9. Between steps 3 and 5, the interface is stretched from 32% (step 3) to 0% (step 4) strain, and then recompressed to 32% (step 5). Between steps 5 and 9, the interface is compressed to 81% strain (step 7), then stretched back to 0% strain (step 8), and recompressed to 32% strain (step 9). Therefore, the interface is compressed to a higher strain between steps 5 and 9 than between steps 3 and 5. This procedure has been described in Table 3-2.

One way to investigate the hysteresis of particle laden interfaces is by looking at the ratio of the area of the interface that has buckled (i.e. that is wrinkled) at a given step of the experimental protocol. This can be measured in ImageJ and is calculated as follows:

$$Q = \frac{\text{area where buckling occurs}}{\text{total area}} \quad (4-9)$$

Note that this is the projected area captured by the camera, and not the developed area of the interface itself. These measurements yield to the data in Figure 4-18.

Interestingly, the change in Q is small between steps 3 and 5, which are characterized by the same strain, but between which the compression is completely released and reintroduced. That indicates that stretching and then re-compressing the interface has little effect on the arrangement of the particles. This is not to say that there is no effect at all; in fact, areas of poor particle coverage often move between steps 3 and 5, and the spatial distribution and alignment of the wrinkles tends to change as well. However, the amount of the interface that is actually buckled does not change, which shows that the effective length of the interface did not change.

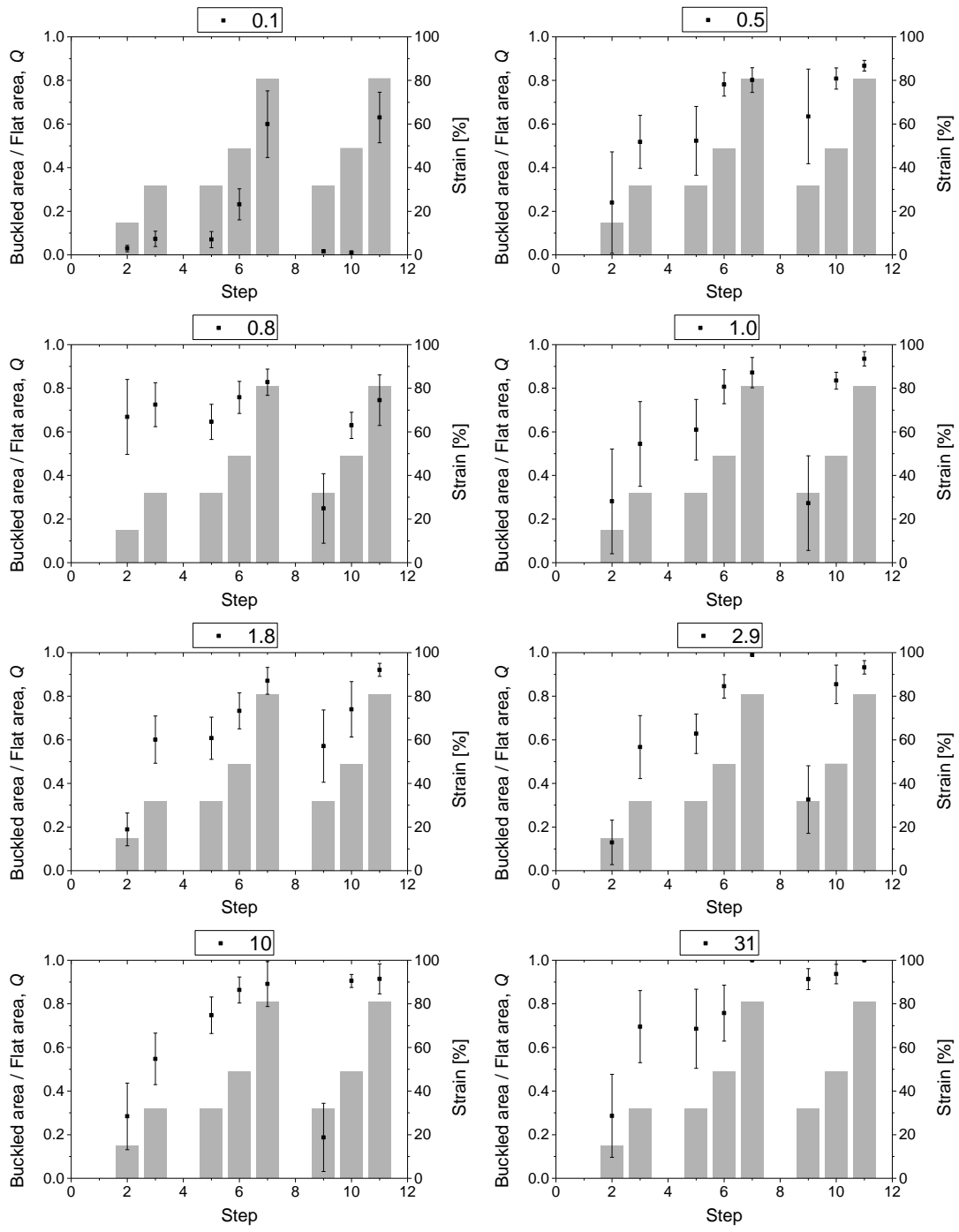


Figure 4-18: The fraction of the particle-laden interface that is buckled (Q , squares) and engineering strain (columns) as a function of step within the experimental protocol, for each particle diameter.

On the other hand, Q tends to be small in step 9, which is at the same strain. It is important to keep in mind that the interface is put under very high strain between steps 5 and 9, which is then released and partially reapplied. The difference in behavior between these two steps thus indicates that high compression can induce changes in particle arrangement. These changes between steps 5 and 9 may be due to:

- a) Forcing closer packing of the particles.
- b) Populating previously unpopulated areas of the trough.
- c) Pushing the particles into the sides of the trough, i.e. away from the zone of unidirectional compression in the middle of the trough.
- d) Irreversible formation of trilayers of particles that effectively reduce the length of the interface.

Items "b" and "c" can be easily investigated through analysis of the images obtained during the experiment, but "a" might require a very close look at the interface, i.e. in conditions that can only be obtained in a scanning electron microscope or similar equipment (with the exception of the largest particles in the present work). Yet, as work with the largest particles used here (lycopodium powder, diameter 31 μm , Figure 4-3) has shown, even large spherical particles tend to be nearly at close packing at the onset of buckling (this is not necessarily the case for irregularly shaped particles, as shown by Horozov et al., 2006). Thus, "a" is unlikely to have contributed to the observed results.

It is also unlikely that "d" played a role, since irreversible trilayers were only observed for the 0.1 μm particles, and even then only on a small portion of the interface. Thus, "b" and "c" are most likely the reason why variations in Q are observed.

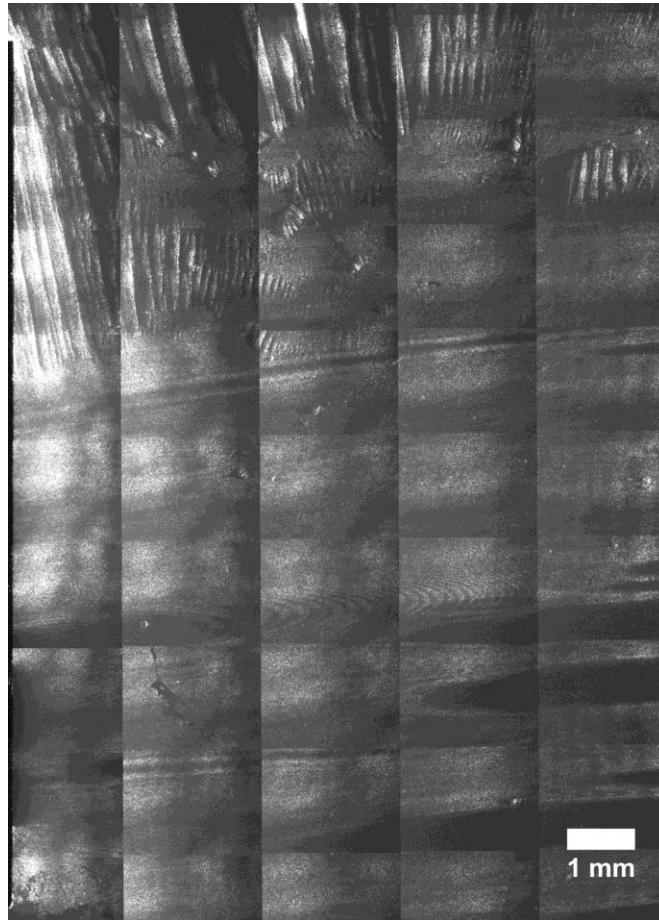


Figure 4-19: 2.9-micron interface at step 1. While buckling occurs at the top part of the image, most of the interface remains flat, indicating that the particle distribution is uneven on the interface.

Indeed, evidence of “b” and “c” can be found on several of the images of the interface, for all particle diameters. For example, buckling is seldom widespread at the beginning of the experiment (see example in Figure 4-19), which indicates a poor distribution of particles on the interface. Thus, it is reasonable to expect that with compression the particles should rearrange in those areas. Note that while a relatively high packing is expected for wrinkles in any particle-laden interface, this discussion refers to

areas where the onset of buckling has not been reached. In those areas, the particles may be very loosely packed, so some displacement of particles toward that particle-poor area is expected.

In some cases, the lack of particles is so pronounced that the empty area can be seen on the picture of the interface, such as in Figure 4-20.

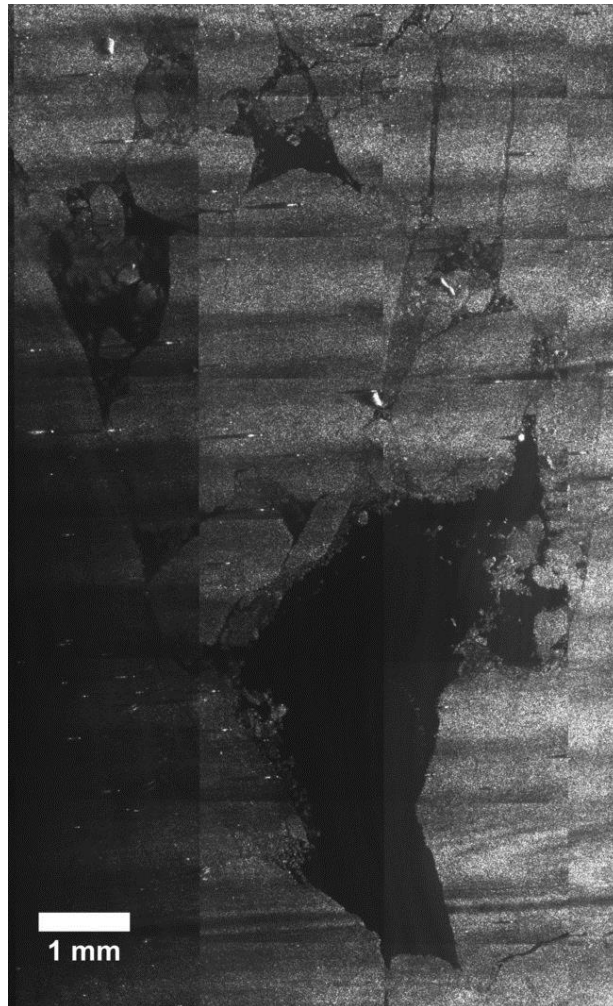


Figure 4-20: 1.0-micron interface at step 1. Regions of particle depletion can be clearly seen as dark areas on the image.

These two phenomena are common in all diameters except 31 μm (lycopodium), which is strong indication that a macroscopic displacement of the particles (“b” or “c”) is likely to be the reason for the observed change in Q . This could be because particle-laden interfaces can resist shear, effectively sheltering particle-poor areas from compression until very high strain is imposed, when the bridge that sustained shear is broken.

The 31 μm particles are an exception because they are sprinkled on top of the interface, rather than injected in solution. That makes the initial spreading more even, reducing the amount of rearrangement that can occur in compression. This also shows that sprinkling, when possible, is a favorable form of depositing particles on the interface.

The consequence of this rearrangement is that particle-laden interfaces tend to become more homogeneous when imposed to large strains. Therefore, the reproducibility of the interfaces increases with the use of hysteresis, which is important both in scientific experiments and in industrial processes.

Yet, it is important to consider whether imposing strain in order to induce hysteresis can also affect the mechanical properties of the interface. Measuring the Young’s modulus directly would be difficult since any measurement technique would introduce strain, but measuring the wavelength as a function of step does not cause that issue. Since the wavelength of buckling is expected to be linked to the mechanical properties of the raft, it can give an indication of the variation of the latter. Figure 4-21 shows the wavelength as a function of step for each of the particle diameters.

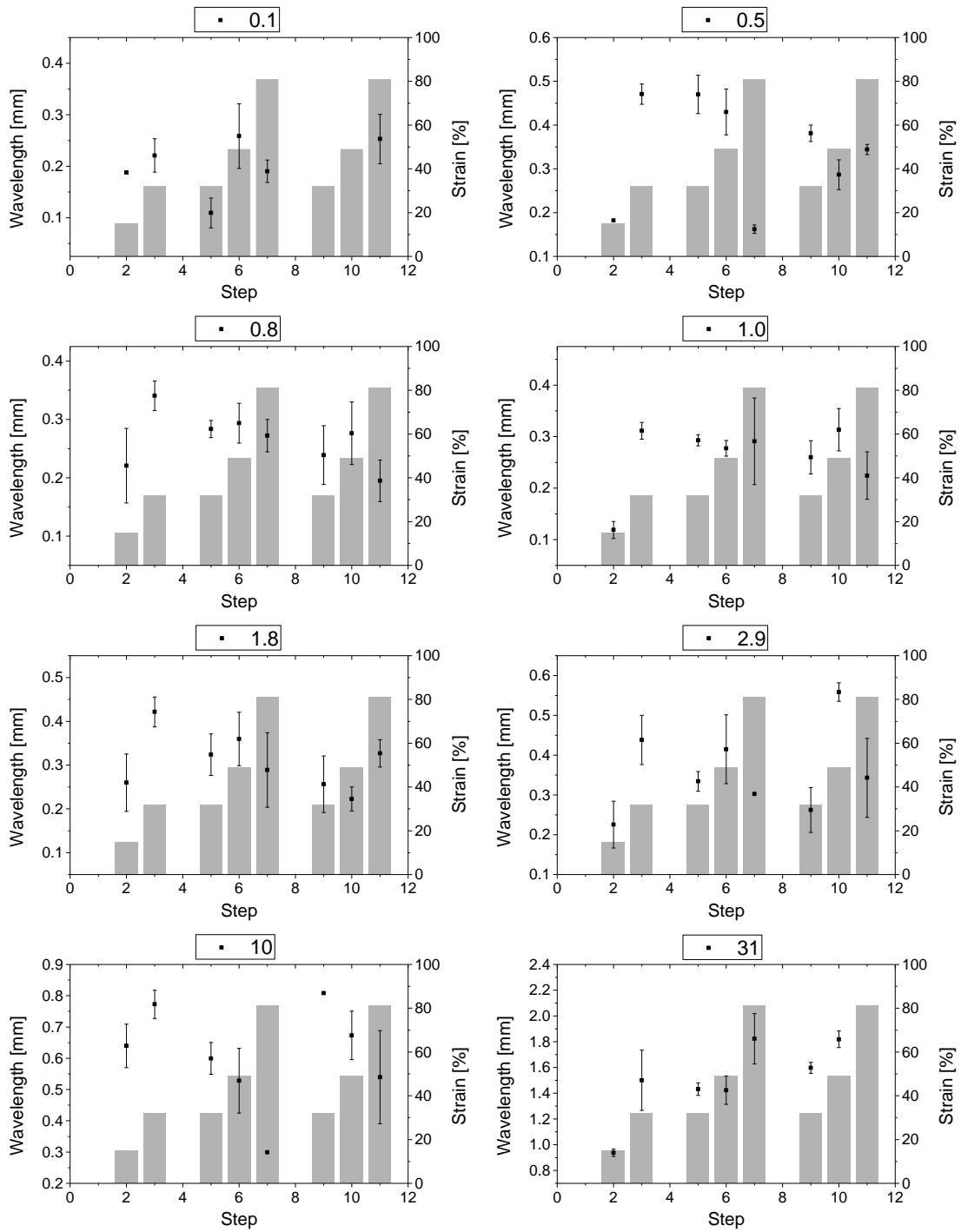


Figure 4-21: Wavelength (squares) and engineering strain (columns) as a function of step for each particle diameter.

While some variation is observed, the wavelength seems to gravitate around the respective average value for all cases shown here. This indicates that the change in bending stiffness, if any, is very small.

As an interesting additional result, in some cases of the 31- μm particles it is clear that the folding of the sheet affected the shape of the wrinkles after folding. This was not detected in any of the other cases; it is likely because the buckling wavelength of the 31 μm -particle rafts is comparable to the length of the trough at the largest strain (81%). In these cases, wrinkling was uneven before folding, but then resolved into very well aligned wrinkles after large deformation was induced on the sheet.

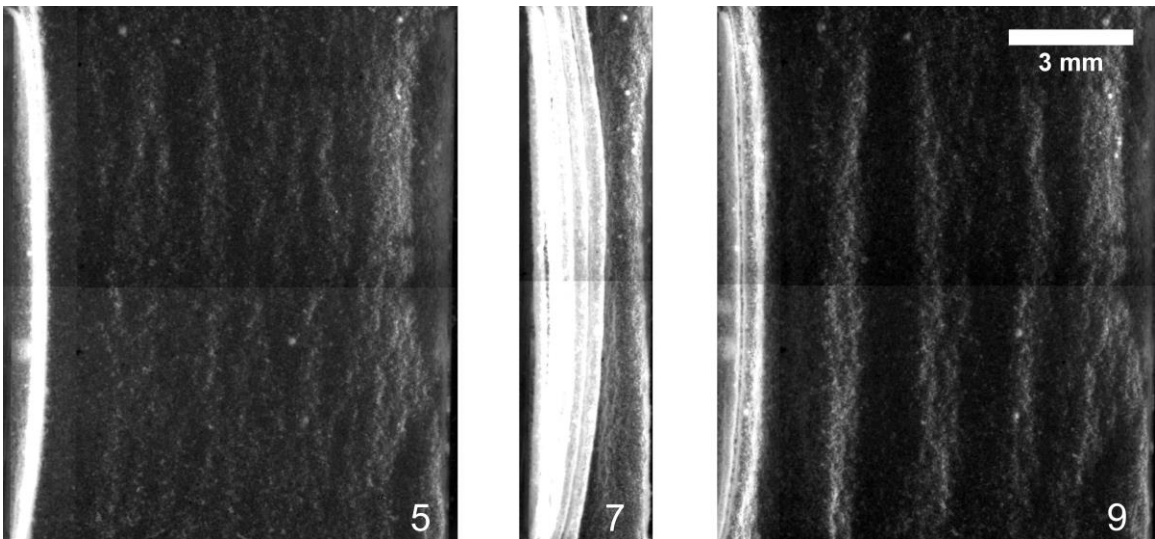


Figure 4-22: 31 μm -particle raft at steps 5, 7 and 9.

Figure 4-22 shows an example of this phenomenon. At step 5, the wrinkles are relatively disorganized. There is some folding near the wall, and small wrinkles on the trough itself. At step 7, the interface has mostly folded as the projected area became very

small. Finally, at step 9 wrinkles form apparently from creases left behind by the folds. This indicates a permanent modification of the structure of the interface.

To sum up, two important points were made in this section of the present work. First, it was shown that compression is an effective way of changing the particle distribution on the interface. This is particularly true for high compressive strains, where substantial changes in distribution may be achieved. Second, the bending stiffness of the interfaces seems largely unchanged by this redistribution, which in turn suggests that the Young's modulus also remains unchanged. That is, insofar as the buckling wavelength correlates to the mechanical properties of the interface, these mechanical properties do not change at the onset of buckling. However, there is also evidence that permanent creasing can occur if compression is extremely large when compared to the wavelength of buckling, as exemplified by the results from the lycopodium particles. As an interesting aside, it was also suggested that sprinkling the particles (as opposed to injecting them in solution) may be a more effective way to obtain homogenous interfaces,

Thus, it can be concluded that successive compression cycles are an effective method of rearranging particles on an interface, particularly if high strains are applied. However, extremely large strains can cause permanent creasing, which may not be desirable. The results suggest that the threshold of creasing is a function of the wavelength of buckling, which in turn is a function of the bending stiffness or the diameter of the particles. Therefore, it is possible that an ideal amount of compression could be devised for a specific geometry or particle diameter in order to maximize the homogeneity of the interface without causing creasing.

CHAPTER 5

CONCLUSION

In the present work, it was shown that the wavelength of buckling of particle-laden interfaces does not follow the trend that has been proposed in the literature. Rather, there is a transition in behavior, such that the wavelength for diameters below the transition is higher than expected. We propose that this occurs because the interface buckles into a trilayer, which has an effectively larger bending stiffness; then, the trilayers buckle at a larger wavelength, leading to the increase in measured wavelength (akin to what has been shown to happen for nanometric gold particles in Leahy et al., 2010). For latex particles adsorbed to a decane-water interface, this transition is in the micron range. However, it is possible that the transition would shift to different diameters depending on the capillary length of the interface.

The suggestion that trilayers are the reason behind the increase in wavelength is supported by the fact that simple mathematical manipulation of the data based on the existing theory allows for the proposed trend to be recovered. Furthermore, if we neglect the points below the transition, the trend is recovered to within experimental error for the points above the micron threshold. Therefore, we propose that the theory presented in Vella et al., (2004) correctly predicts the trend in buckling wavelength as a function of particle diameter for decane-water interfaces with particle diameters larger than 1 μm , and that it can be corrected to account for diameters below that value. This extends the proven range of that theoretical framework to a liquid-liquid interface.

It was also shown that different wavelengths can occur at different areas of a particle-laden interface. Interestingly, the transition between different wavelengths can

take place through cascading, as in thin solid sheets. Both “light” and “heavy” sheet behavior are possible, but the latter is observed to occur more often. However, the area of the transition is usually small, so the expected trends are not always recovered.

The transition between different wavelengths within a buckled raft has also been shown to occur in completely novel ways. In one of those cases, a flat area remains between two trains of wrinkles, allowing for the misalignment of the crests. Another possibility is that a very pronounced discontinuity may form along the raft, with different wavelengths on either side. Lastly, wrinkles were also observed to split into up to six smaller wrinkles. None of these cases has been reported in thin solid sheets, to the best of our knowledge.

Another important conclusion is that compression can be used effectively to change the particle distribution on the interface from a macroscopic perspective, especially if large compressive strains are imposed on the particle raft. This could be particularly useful in applications where the particles must be injected (as opposed to sprinkled) on the interface. The small changes in wavelength between compression cycles suggest that the bending stiffness of the interface remains unchanged by the process. However, the results for lycopodium particles show that very large compressions can lead to permanent creasing, suggesting that the amount of strain must be tuned to the geometry of the raft and the bending stiffness of the interface.

APPENDIX

C++ CODE

A C++ console program was written in order to measure the wavelength of the wrinkles on the particle-laden interface. The program was based on the fact that when illuminated with a nearly horizontal laser sheet, the wrinkles appear more clearly on the side facing the laser and darker on the side facing away from the laser. Consequently, the dark areas fall below a certain threshold value, while the light areas do not. By calculating the distance between two successive dark areas, one can obtain the approximate wavelength between two wrinkles.

The program must scan the image progressively, either along the y -axis or the x -axis. Since the images were taken such that the direction of compression was aligned with the x -axis, the raster scanning was done along each row successively. Therefore, the measured distance is not exactly the wavelength of the wrinkles, which is the distance between two crests when measured perpendicularly to the crest, but rather the distance between the crests along the x -direction. Since the wrinkles are not always perfectly aligned with the direction of compression (as shown in several cases in the present work, e.g. Figure 4-6), some form of correction for this error is necessary.

Simple geometry shows that for a given distance L along the x -axis, there is a corresponding wavelength λ that is a function of the angle of the crest to the x -axis, such that:

$$\lambda = L \sin \theta \quad (6-1)$$

Naturally, this means the angle θ must be calculated. This angle is the slope of the crest about the x -axis (see Figure 6-1), which means at least two points must be used in its calculation. This adds complexity to the program, because now it must be able to tell when two points are part of the same crest or not, which was not necessary before.

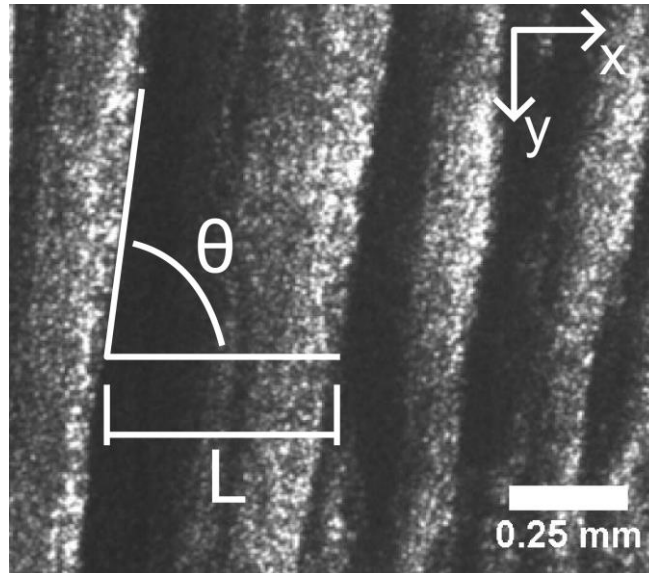


Figure 6-1: Parameters for calculating the buckling wavelength; 2.9 μm -particle raft.

To simplify this process, a C++ class was created to represent the crests of wrinkles. Each crest that is detected on an image is represented as a separate instance of that class. The class also contains the methods and members pertinent to the calculations done here, such as finding the points on the image that are part of the crest and calculating the slope θ .

In order to find out which points are part of a certain crest, each point on an image that bordered an area below the threshold is marked as an edge and assigned the measured

distance L pertaining to that particular point. Then, the image is scanned to identify which edges are part of the same crest. The scanning is done by finding an edge at the top of the image and looking at the points surrounding that edge within a certain tolerance. If other edges are found within the tolerance, they are added to the crest and a new search area is defined based on the position of the recently added edges. In other words, the crest object (instance of the crest class) that represents that crest is fed with the new data points and the new search area is calculated based on the position of those data points.

If no edges are found within the search area, the crest is assumed to have been entirely detected and the program moves on to calculating the slope. This is done by applying a least squares fit to the coordinates of the edges contained in the crest object. Then, the slope of that fit is the desired angle θ and Equation (6-1) can be used to calculate the corrected wavelength.

Under ideal circumstances with perfect lighting, the wavelength can be calculated to the accuracy offered by the resolution of the image. However, lasers are prone to generating speckle noise and the particles themselves are scattered reflectors, so the images tend to be very speckled. Because of that, a number of different treatments were attempted in order to reduce the speckle noise before the image processing program was run. Fourier transform filters and averaging filters are both reasonably effective at removing speckle noise.

Another issue is that the contrast in real images may be really small, which would make it difficult to obtain a measurement of wavelength. Enhancing contrast by renormalizing an image is effective at solving this issue, as is the built-in “Shadows” filter

in ImageJ. It should be noted that enhancing contrast can only be done after de-speckling, otherwise speckling will become even worse.

If caution is used in order to avoid the issues with noise, the image processing program yields good results, for example Figure 4-13. Nevertheless, sample measurements by hand are also carried out to ensure that the output of the program is consistent.

Despite requiring time to pre-process the images and post-process the data, as well as to take sample measurements by hand, the image processing program allowed for a very large amount of data to be acquired in a timely fashion, which would have been impossible otherwise.

BIBLIOGRAPHY

- Ashby, N. P., & Binks, B. P. (2000). "Pickering emulsions stabilised by Laponite clay particles". Physical Chemistry Chemical Physics, **2**(24), 5640–5646.
- Aveyard, R., Clint, J. H., Nees, D., & Paunov, V. N. (2000). "Compression and Structure of Monolayers of Charged Latex Particles at Air / Water and Octane / Water Interfaces". Langmuir, **16**(13), 1969–1979.
- Aveyard, R., Clint, J. H., Nees, D., & Quirke, N. (2000). "Structure and Collapse of Particle Monolayers under Lateral Pressure at the Octane / Aqueous Surfactant Solution Interface". Langmuir, **16**(8), 8820–8828.
- Binks, B. P. (2002). "Particles as surfactants - similarities and differences". Current Opinion in Colloid & Interface Science, **7**(1-2), 21–41.
- Birdi, K. S. (1994). Handbook of Surface and Colloid Chemistry (2nd ed.). Boca Raton, London, New York, Washington, D. C.: CRC Press.
- Birdi, K. S. (1999). Self-Assembly Monolayer Structures of Lipids and Macromolecules at Interfaces (1st ed.). New York: Springer.
- Bloom, F., & Coffin, D. (2000). Handbook of Thin Plate Buckling and Postbuckling (1st ed.). Boca Raton: Chapman and Hall/CRC.
- Boneva, M. P., Christov, N. C., Danov, K. D., & Kralchevsky, P. A. (2007). "Effect of Electric-Field-Induced Capillary Attraction on the Motion of Particles at an Oil-Water Interface". Physical chemistry chemical physics, **9**, 6371–6384.
- Danov, K. D., Kralchevsky, P. a, & Boneva, M. P. (2004). "Electrodipping force acting on solid particles at a fluid interface.". Langmuir : the ACS journal of surfaces and colloids, **20**(15), 6139–51.
- De Gennes, P.-G., Brochard-Wyart, F., & Quere, D. (2003). Capillarity and Wetting Phenomena: Drops, Bubbles, Pearls, Waves (2004th ed.). New York: Springer.
- Dinsmore, A. D., Hsu, M. F., Nikolaidis, M. G., Marquez, M., Bausch, A. R., & Weitz, D. A. (2002). "Colloidosomes: Selectively Permeable Capsules Composed of Colloidal Particles". Science, **298**(5595), 1006–1009.
- Du, K., Glogowski, E., Emrick, T., Russell, T. P., & Dinsmore, A. D. (2010). "Adsorption energy of nano- and microparticles at liquid-liquid interfaces". Langmuir, **26**(15), 12518–12522.

- Edmond, K. V., Schofield, A. B., Marquez, M., Rothstein, J. P., & Dinsmore, A. D. (2006). "Stable jets of viscoelastic fluids and self-assembled cylindrical capsules by hydrodynamic focusing". Langmuir, **22**(21), 9052–9056.
- Helseth, L. E., Muruganathan, R., Zhang, Y., & Fischer, T. M. (2005). "Colloidal Rings in a Liquid Mixture". Langmuir, **21**(16), 7271–7275.
- Horozov, T. S., Binks, B. P., Aveyard, R., & Clint, J. H. (2006). "Effect of Particle Hydrophobicity on the Formation and Collapse of Fumed Silica Particle Monolayers at the Oil–Water Interface". Colloids and Surfaces, **282-283**, 377–386.
- Huang, J., Davidovitch, B., Santangelo, C. D., Russell, T. P., & Menon, N. (2010). "Smooth Cascade of Wrinkles at the Edge of a Floating Elastic Film". Physical Review Letters, **105**(3), 038302–1–4.
- Kang, Z., Yeung, A., Foght, J. M., & Gray, M. R. (2008). "Mechanical Properties of Hexadecane-Water Interfaces with Adsorbed Hydrophobic Bacteria". Colloids and Surfaces, **62**(2), 273–279.
- Leahy, B. D., Pocivavsek, L., Meron, M., Lam, K. L., Salas, D., Viccaro, P. J., ... Lin, B. (2010). "Geometric Stability and Elastic Response of a Supported Nanoparticle Film". Physical Review Letters, **105**(5), 058301(4).
- Libby, L. M., Libby, W. F., & Lawrence, S. S. (1969). "Measurement of Ocean Waves in a Satellite Photograph". RAND Corporation.
- Monteux, C., Jung, E., & Fuller, G. G. (2007). "Mechanical Properties and Structure of Particle Coated Interfaces: Influence of Particle Size and Bidisperse 2D Suspensions.". Langmuir, **23**(7), 3975–3980.
- Monteux, C., Kirkwood, J., Xu, H., Jung, E., & Fuller, G. G. (2007). "Determining the Mechanical Response of Particle-Laden Fluid Interfaces Using Surface Pressure Isotherms and Bulk Pressure Measurements of Droplets". Physical chemistry chemical physics, **9**, 6344–6350.
- Mulligan, M. K. (2012). "Morphology and Development of Droplet Deformation Under Flow Within Microfluidic Devices". University of Massachusetts Amherst.
- Paunov, V. N. (2003). "Novel Method for Determining the Three-Phase Contact Angle of Colloid Particles Adsorbed at Air - Water and Oil - Water Interfaces". Langmuir, **19**(19), 7970–7976.
- Pickering, S. U. (1907). "Emulsions". Journal of the Chemical Society, **91**, 2001–2021.
- Ramsden, W. (1903). "Separation of Solids in the Surface-Layers of Solutions and "Suspensions" (Observations on Surface-Membranes, Bubbles, Emulsions, and

- Mechanical Coagulation)". Proceedings of the Royal Society of London, **72**, 156–164.
- Reynaert, S., Moldenaers, P., & Vermant, J. (2006). "Control over Colloidal Aggregation in Monolayers of Latex Particles at the Oil – Water Interface Control over Colloidal Aggregation in Monolayers of Latex Particles at the Oil - Water Interface". Langmuir, **22**(11), 4936–4945.
- Vandeparre, H., Piñeirua, M., Brau, F., Roman, B., Bico, J., Gay, C., ... Damman, P. (2011). "Wrinkling Hierarchy in Constrained Thin Sheets from Suspended Graphene to Curtains". Physical Review Letters, **106**(22), 224301(4).
- Vella, D. (2007). "The Fluid Mechanics of Floating and Sinking". University of Cambridge.
- Vella, D., Aussillous, P., & Mahadevan, L. (2004). "Elasticity of an interfacial particle raft". Europhysics Letters (EPL), **68**(2), 212–218.
- Vella, D., & Mahadevan, L. (2005). "The “Cheerios Effect”". American Journal of Physics, **73**(9), 817–825.
- Vinson, J. R. (1988). The Behavior of Thin Walled Structures: Beams, Plates, and Shells (Mechanics of Surface Structure) (p. 182). Springer.